IEEE Transactions on Nuclear Science, Vol. NS-26, No. 2, April 1979

CONSIDERATIONS FOR THE DESIGN OF A TIME PROJECTION LIQUID ARGON IONIZATION CHAMBER*

E. Gatti, G. Padovini, L. Quartapelle†

and

N. E. Greenlaw and V. Radeka‡

ABSTRACT

Basic concepts of electrode geometry and signal processing for a time projection liquid argon ionization chamber are introduced. The design criteria of a system of sensing electrodes are discussed. The signals induced by rectilinear particle tracks on the sensing electrodes are calculated by means of a detailed study of possible electric field configurations. Suitable signal processing filters are designed in order to achieve nearly equal position resolution in the three space coordinates. The electronic noise limits the position resolution of a single track to a few tenths of a millimeter and the capability to resolve and measure closely spaced multiple tracks to a few millimeters.

CONTENTS

LIST OF SYMBOLS

A	area of F(t)	[volt sec]
A_o	area of $F_o(t)$	[volt sec]
A_r	area of $F_r(t)$	[volt sec]
A_{ro}	area of $F_{ro}(t)$	[volt sec]
C	capacitance of a sensing wire plus input capacitance of the associated amplifier	
C_w	capacitance between a sensing wire and a neighboring one	
C_k	capacitance between a sensing wire and a sensing wire of the other plane	
D	diffusion coefficient	
d	ionization density of a track	
E_{as}	asymptotic field	
e_n^2	unilateral (physical) noise spectral density	$[V^2/Hz]$
F(t)	voltage waveform induced by a track	[volt]
$F_o(t)$	voltage waveform induced by a track parallel to the grid planes	
$F_r(t)$	voltage waveform induced by a track when the reference induced charge waveform $f_r(h,t)$ is used	
$F_{ro}(t)$	voltage waveform induced by a track parallel to the grid planes when the reference induced charge waveform $f_r(h,t)$ is used	
f(h,t)	induced charge waveform on a sensing wire due to a unit charge starting at distance h from the considered wire (see Fig. 2.7)	
$f_r(h,t)$	reference induced charge waveform (Fig. 5.2)	
G	spacing between grid planes	
g(t)	filter's δ-response	
H(s)	filter transfer function	
h	distance of a point charge from the center of a sensing wire in the y direction	
L	r.m.s. width of F(t)	
L_o	r.m.s. width of $F_o(t)$	
L_s	r.m.s. width contribution due to the inclination of the track	
m	normalized peak amplitude of the filter	
m'	dimensionless peak amplitude of the filter	
N(q)	cumulative probability density for tracks giving rise to input current pulses with a normalized charge lower than q	
N(λ)	cumulative probability density for tracks giving rise to input current pulses with a normalized width lower than λ	
n	normalized slope of the filter	
n'	dimensionless slope of the filter	
p	weighting coefficient for the effective Green function	

*This research was supported in part by the U. S. Department of Energy: Contract No. EY-76-C-02-0016 and in part by Istituto Nazionale di Fisica Nucleare.

†Istituto di Fisica Politecnico di Milano, Milano, Italy.

‡Brookhaven National Laboratory, Upton, New York 11973.

Manuscript received by NPSS Sept. 18, 1978.

Q_{2w}	charge of the "input current pulse"
Q_o	Q_o = 2dw charge of the "input current pulse" for $\theta = \varphi = \pi/2$, i.e., track perpendicular to the wires
q	$q = Q_{2w}/Q_o$ normalized charge of an input pulse
R	wire radius
S	zero crossing slope of W(t)
T	width of the rectangular "input current pulse"
T_D	width at the base of the reference waveform $f_r(h,t)$
T_M	total width of a filter's δ-response
T_r	time necessary for an electron to travel a distance 2 w
t_o	zero crossing time of the waveform W(t)
t_c	centroid of F(t)
u	saturated drift velocity of electrons
V_A	anode potential; (V_A = 0, anode plane simulates second sensing grid array)
V_S	first sensing grid potential
V_G	screen grid potential
W(t)	filter's output waveform response to F(t)
$W_r(t)$	filter's output waveform response to $F_r(t)$
W_{max}	peak value of W(t)
w	wire spacing
Z	r.m.s. noise to peak signal ratio
α	$\alpha = A/A_r = A_o/A_{ro}$
β	$\beta = T_D/L_o$
ξ	$\xi = T/L_s$
λ	$\lambda = T/T_r$ normalized width of an input pulse
e_N^2	mean squared voltage noise
e_t^2	timing variance
e_x^2	space resolution variance
θ,φ	polar angular coordinates of a track

* * * * * * * * * * * * * * * * *

Subscripts 1 and 2 refer to the first and the second filter, respectively.

1. Introduction

The purpose of the imaging device under consideration is the reconstruction by electrical signals of the geometry of a high energy event taking place in the sensitive volume of a time projection liquid argon ionization chamber. The idea consists of drifting the whole electron image of an event occurring in liquified noble gas onto an array of sensing electrodes, which are arranged so that the three-dimensional image of the event can be reconstructed from the two coordinates of the image projection in the electrode plane and from the drift time.

The idea has evolved as follows. In 1969, Charpak et al.[1] showed that the three coordinates of primary ionization in a gas drift chamber can be determined from the electron drift time to an anode and from the two coordinates of the avalanche in the anode plane, and they suggested a three dimensional (avalanche) chamber. In 1974, Nygren[2] proposed the time projection chamber (TPC) based on these principles, in which the reconstruction of multiprong events and their identification from the energy loss ($\Delta E/\Delta X$) in gas can be performed. In 1975, W. J. Willis suggested to one of the authors (V. R.) the idea of the time projection chamber in liquified noble gases which led to the developments described in this paper. In 1977, Rubbia[3] described some basic features of a liquid argon time projection chamber.

There is a significant difference in the signal size between the chamber using amplification in gas and the chamber with liquified noble gas, where amplification has not proved practical and the signals produced by the primary ionization have to be detected. The problem of obtaining maximum information for particle track reconstruction from the small amounts of ionization in the chamber is the main subject of this paper. The basic concepts of optimum electrode geometry and signal processing for time projection ionization chambers are introduced here.

The realization of such a chamber depends on the ability to drift electrons in liquid argon over long distances. Encouraging results have been obtained by Chen et al.[4]

The dimensions of the ionization chamber are set by the nature of the application and the attainable drift distance. For use as a vertex detector for high energy physics experiments, the approximate dimensions should be 20 x 20 x 50 cm, with the incident beam along the largest dimension, and the expected resolution for minimum ionizing particle of a fraction of a millimeter. For a large volume detector, as for neutrino experiments, the cross section should be several square meters, and the drift distance as long as allowed by electron attachment and a practical drift field. In this case, resolution would be several millimeters.

As an example with strong requirements on resolution, we consider here an ionization chamber having dimensions 20 x 20 x 50 cm (last dimension taken parallel to the primary beam). The electrons, produced by and defining the pattern of the event, drift in a uniform electric field and are sensed as induced charge by a system of wires placed beyond a screen grid. The wires sensing the signals give, by their own position, two coordinates perpendicular to the electric field while the timing of the signals gives information about the coordinate parallel to the drift field.

A solution with a point array of sensing electrodes has been disregarded because it would imply an unacceptably large number of high quality amplifiers and electrode connections of the order of 200 x 200 for the required resolution. Alternatively, sensing electrodes consisting of two crossed sets of parallel wires lying in parallel planes will be considered here. With a wire spacing of 1 mm, this solution implies the use of (200 + 200)

amplifiers. One is faced, however, with the well known problem of ghost events when the coordinates of more than one electrode intersection have to be recorded simultaneously, and this will happen frequently for the ionization chamber under consideration. The problem is generally solved (for a limited amount of multiplicity) with a third layer of wires inclined with respect to the other two sets. However, if the chamber is used to image multiparticle jets radiating from a narrow primary beam, and if the ionization pattern is made to drift in a direction parallel to the beam, then a better geometry (at least for not too large track curvature) for the third set of sensing electrodes might be circular sectors as shown in Fig. 1.1, or a rough checkerboard of about one hundred electrodes.

In spite of the fact that hydrogen is often a more interesting target, this first design is based on argon for two reasons:

- the larger ionization density for particles at minimum of ionization (8000 pairs/mm);
- the experience with liquid argon ionization chambers existing at Brookhaven National Laboratory and CERN.

For this liquid the saturated electron velocity u is about 5×10^3 m/s for an electric field larger than 200 volt/mm, or 100 kV for a chamber 50 cm long. Maximum drift time will be about 100 μs. This is quite large and imposes severe restrictions on event rate, in order to have no more than one ionization pattern at a time present in the chamber on the average.

Drifting in a direction perpendicular to the primary beam could also be considered and, of course, maximum drift time would be reduced to 40 μs and total voltage to 40 kV. (In this case, the third group of sensing electrodes would be parallel wires.)

Resolution of the chamber will also be limited by diffusion. Inserting into the Einstein relationship an electron energy of 0.1 eV for $E = 2 \times 10^5$ volt/m as a rough estimate, and taking $\mu = 4 \times 10^{-2}$ $m^2/volt_s$, we estimate a diffusion coefficient $D = 4 \times 10^{-3}$ m^2/s and a standard deviation of ~ 0.6 mm after 100 μs drift time. Of course, this figure has to be considered only as an order of magnitude estimate. A better evaluation needs experimental values for longitudinal and transversal diffusion as a function of the electric field and impurities.

Electron drift for lengths up to 35 cm in liquid argon has been already experimentally demonstrated.[4]

As the three cascaded sets of sensing electrodes are provided, the first two must not collect the drifting electrons but merely sense the signals as induced charges. The proposed geometry is shown in Fig. 1.2. (The last set of sensing electrodes in the form of circular sectors is not shown.) Wire spacing w, wire radius R, and spacing G between grid planes are chosen according to considerations presented in this paper.

In order to estimate the resolution capability of the device, we consider here the simplest case, that is the one of a rectilinear track of uniform density d (Landau fluctuations are neglected) with a given orientation θ, φ in space. We have calculated the accuracy of the timing information available from the signal induced on a sensing wire by the relevant portion of the track drifting through the screen grid and passing in the vicinity of the sensing wire. (The problem of measuring the ends of tracks or processing of peculiar signals due to the ionization first formed beyond the screen grid is not considered here.)

The electrostatic problem has been studied to calculate the electric field and the corresponding electron trajectories for a given geometry. The necessary conditions are that the electron trajectories should not fall on the grid wires and that nearly all electrons move at the saturation velocity. The induction weighting function, that is the harmonic Green function equal to 1 at the sensing wire considered and 0 at all other electrodes, has been used to calculate the charge pulse induced at the wire from the known laws of electrons of motion along their trajectory.

To design the most suitable filters to be used in connection with charge sensitive low noise amplifiers, idealized reference waveforms for the charge pulse have been introduced as a rough approximation to the exact ones. Focusing of the screen grid has been neglected and a weighting function of triangular shape, linearly decreasing in amplitude with the distance h from the sensing wire, has been assumed. (Compare Fig. 5.1 with Fig. 2.6(b) and Fig. 6.2 with Figs. 2.9(a) and (b)).

This paper, while studying in detail the signals from a point of view of the time and position information which can be extracted, does not enter into the problems of digital processing and the organization of the large amount of information arising from the sensing wires in order to reconstruct the ionization patterns.

2. Potential and Field, Induced Pulse Shape, and Electrode Capacitances

In order to study induced charge pulses we have to find for the considered geometry and the assigned potential values at the electrodes: i) the lines of the electric field in the chamber from which the law of motion of the inducing charge may be derived; ii) the weighting Green function of the sensing wire which allows us to calculate the induced charge as a function of the position of the inducing charges.

The electric field and all related parameters of the chamber have been computed with reference to the idealized geometry shown in Fig. 2.1. Both the screen grid and the first sensing grid have been assumed to consist of an infinite number of straight wires of infinite length and given radius. The second sensing wire array, perpendicular to the first one, is approximated by a plane anode. With these assumptions we are led to a periodic problem in two dimensions which can be dealt with by means of the complex potential formalism. This method has the advantage of providing both the potential function and the field line function we need in order to calculate the trajectories of the electrons under the assumed condition of saturated velocity.

The analytical solution of the electrostatic problem of an infinite array of uniformly charged lines with equal spacing was found by J. C. Maxwell[5] by means of the logarithmic conformal mapping of the potential of a single uniformly charged line (see also Refs. (6),(7)). To match the boundary conditions imposed by the finite radius of the circular wires we have considered two additional terms in the multipole expansion of the potential, i.e., a dipole and a quadrupole placed at the position of the line and with orientation dictated by symmetry. By

applying the conformal mapping to these contributions, too, we obtain all the contributions to the complex potential which are respectively for charge, dipole and quadrupole

$$V_C = a_C \ln\{1/[\cosh(s-x_o) -1]\} \quad ,$$

$$V_D = a_D[\sinh(s-x_o) -1]/[\cosh(s-x_o) -1] \quad , \qquad (2.1)$$

$$V_Q = a_Q\, 1/[\cosh(s-x_o) -1] \quad ,$$

where $s = x + iy$, x_o is the distance of the grid plane from the origin and the a's are coefficients to be determined.

To assure a constant potential at the anode plane, (for convenience we choose this constant potential V_A equal to zero) we assume it as a symmetry plane and introduce mirror multipole contributions. They are directly obtained from the above relations by changing x_o into $-x_o$, a_C into $-a_C$, a_Q into $-a_Q$ while a_D remains unchanged. Obviously, the total complex potential must include contributions due to the sensing grid and the screen grid which correspond to terms with $x_o = G$ and $x_o = 2G$, respectively.

Furthermore, a linear term

$$V_L = a_L s \qquad (2.2)$$

must also be added to account for the uniform asymptotic field E_{as} in the chamber.

To calculate the influence coefficients needed to determine the unknowns, we must fix a number of points (equal to the number of the a's) where the value of the potential is assigned and chosen in such a way to provide a solution for the potential which gives satisfactory approximation to the circular shape of the wires (see Fig. 2.2). The field configuration is then obtained by solving the linear system for the a's once the values of the potential at the electrodes are given. The field lines and associated potential distribution are shown in Figs. 2.3 and 2.4 for two different sets of potentials (a) and (b) given to the chamber electrodes. In both cases the screen grid has such a potential as not to collect electrons (or field lines coming from the cathode). In the case (a) the sensing grid is placed at the geometrical potential and does not distort appreciably the above mentioned field lines which have been focused by the screen grid in the central zone between the adjacent sensing wires. As it may be expected, this situation, apparent in Fig. 2.3, is characterized by a shrinkage factor of the field lines equal to the ratio of the asymptotic electric fields downstream and upstream the screen grid.

On the contrary, in case (b) the potential of the sensing grid is so chosen as to counterbalance the focusing action of the screen grid, i.e., the field lines focused in the central region by the screen grid are defocused by the sensing grid so that the initial uniform distribution is restored (see Fig. 2.4). In this case the third grid (second sensing grid with wires orthogonal to the ones of the first two grids) would not be affected, as far as the z, y coordinates are concerned, by the pattern deformation due to the focusing effect of the screen grid.

Moreover, this second case has the advantage of restoring the electric field after the first sensing grid to the value E_{as} present in the drift space of the ionization chamber. If the second sensing grid must not capture electrons, it is sufficient to double the electric field E_{as} in the region between this grid and the anode (4th set of electrodes).

Let us now consider the problem of calculating the Green function V of a signal wire of the sensing grid. This means to solve the potential problem with the following Dirichlet boundary conditions: potential equal to 1 at the chosen sensing wire and equal to zero at all the remaining boundaries. Since these boundary conditions are not periodic in y-direction, we must resort to direct summation of multipole contributions coming from a large number of distinct wires. In practice, we have found a satisfactory representation of the circular shape of the sensing and screen wires in the region of interest by taking into account for each wire a number of multipole terms dependent on its position with respect to the sensing wire. For the central wire we have considered the charge term and the dipole and quadrupole terms with orientation dictated by the symmetry of the problem,

$$V_1 = b_1 \ln\{1/[(x-x_o)^2 + y^2]^{\frac{1}{2}}\} \quad ,$$

$$V_2 = b_2(x-x_o)/[(x-x_o)^2 + y^2] \quad , \qquad (2.3)$$

$$V_3 = b_3[(x-x_o)^2 - y^2]/[(x-x_o)^2 + y^2]^2 \quad .$$

For the wire adjacent to the central one we have considered the charge term, two perpendicular dipole terms, and a quadrupole term whose orientation has been chosen to approximate the true one.

$$V_4 = b_4 \ln\{1/[(x-x_o)^2 + (y-w)^2]^{\frac{1}{2}}\} \quad ,$$

$$V_5 = b_5(x-x_o)/[(x-x_o)^2 + (y-w)^2] \quad , \qquad (2.4)$$

$$V_6 = b_6(y-w)/[(x-x_o)^2 + (y-w)^2] \quad ,$$

$$V_7 = b_7[(x-x_o)^2 - (y-w)^2]/[(x-x_o)^2 + (y-w)^2]^2 \quad .$$

For the next 9 lateral wires we have taken into account only the charge terms

$$V_\ell = b_\ell \ln\{1/[(x-x_o)^2 + (y-(\ell-b)w)^2]^{\frac{1}{2}}\} \quad , \qquad (2.5)$$

$$\ell = 8,9 \ldots ,16 \quad .$$

The expressions (2.4) and (2.5) refer only to the wires placed on one side of the symmetry plane y = 0 so that the corresponding expressions for the contributions coming from the wires placed on the other side must also be included. They are obtained from changing w into - w and reversing the sign of the y-oriented dipole contribution.

Again, the vanishing of the potential at the anode plate requires to include mirror contributions. This is

easily performed by using the above relations with x_o changed into $-x_o$ and b_ℓ changed into $-b_\ell$ for all ℓ different from 2 and 5. Finally, the contribution coming from the two grids must be considered. This is easily done by taking the above expressions with $x_o = G$ for the sensing grid and with $x_o = 2G$ for the screen grid.

As for the 32 boundary points, to impose the assigned boundary values of the Green function, we have relied upon the choice shown in Fig. 2.5 which gives an accurate description of the circular shape of the wires in the region where the Green function differs significantly from zero. A plot of the calculated Green function is given in Fig. 2.6(a).

As the Green function spreads too much in y direction leading to a poor spatial resolution along this coordinate, a better space behavior can be obtained by an "effective Green function". This is given by the following linear combination of Green functions of the three neighboring wires,

$$V(x,y) + p[V(x,y+w) + V(x,y-w)] \quad , \tag{2.6}$$

where the weight p has been chosen equal to -0.3 (see Fig. 2.6(b)).

The induced charge waveform f(h,t) due to a unit charge starting to move at a given h (Fig. 2.7) is obtained by following with constant velocity the involved field line through the sensing region to the anode, and by evaluating at each time the induced charge by means of the values of the effective Green function at the corresponding point. The result is shown in Figs. 2.8(a) and (b). The total charge pulse due to an infinite track of uniform ionization density is obtained by superposition of the calculated contributions, taking into account for inclined tracks the proper time displacement of the contributions (Figs. 2.9(a) and (b)).

The electrostatic calculations for obtaining the Green function lead automatically to the evaluation of the equivalent capacitances of the sensing wires which are given in Fig. 8.1 for an assumed length of 20 cm.

3. "Input Current Pulse"

Let us introduce the concept of an "input current pulse", due to a rectilinear track direction θ and φ (see Fig. 1.2) for a definite sensing wire. We define this input current pulse as the current which would be produced by the electrons of the rectilinear track crossing a reference width 2w of the screen surface, just above the sensing wire under consideration, if the electric drifting field were uniform (the focusing effect of the screen grid and contributions of electrons crossing the grid on either side of the reference surface of width 2w will be taken into account separately).

By definition, the "input current pulses" are rectangular and may be defined by their total charge

$$Q_{2w} = \int_o^T i\,dt \quad \text{and by their width T.}$$

Q_{2w} and T are calculated by the following geometrical considerations.

Consider as a reference case the one in which the track is parallel to the screen grid plane but perpendicular with respect to its wires (Fig. 3.1). In this case ($\theta = \varphi = \pi/2$)

$$Q_{2w} = Q_o = 2w \cdot d \qquad T = 0 \quad . \tag{3.1}$$

If the track is parallel to the screen grid plane ($\theta = \pi/2$) and has an angle $\varphi \neq \pi/2$ with respect to the screen wires, (Fig. 3.2) we have

$$Q_{2w} = 2\ell d = \frac{2wd}{|\sin\varphi|} = \frac{Q_o}{|\sin\varphi|} \quad , \qquad T = 0 \quad . \tag{3.2}$$

Finally, if the track has direction θ and φ as shown in Fig. 3.3, then

$$Q_{2w} = 2\ell d = \frac{2\ell' d}{|\sin\theta|} = \frac{2wd}{|\sin\varphi||\sin\theta|} = \frac{Q_o}{|\sin\varphi||\sin\theta|} \quad , \tag{3.3}$$

$$T = \frac{n}{u} = \frac{2\ell|\cos\theta|}{u} = \frac{2w}{u}\,\frac{1}{|\sin\varphi\,tg\theta|} = \frac{T_r}{|\sin\varphi\,tg\theta|} \quad , \tag{3.4}$$

where reference time $T_r = 2w/u$ is the time necessary for an electron to travel a distance 2w.

4. Probability Densities of Input Pulses Having Given "Input Charge Q_{2w}" and "Input Current Pulse Width T"

It is now useful to calculate the probability densities of getting "input pulses" of normalized charge $q = Q_{2w}/Q_o$ and of normalized width $\lambda = T/T_r$ under the simple hypothesis of tracks isotropically distributed in space. This leads to a track density per unit solid angle equal to $1/4\pi$.

In order to calculate the fraction of tracks which give rise to a normalized charge lower than q, it is sufficient to calculate the cumulative probability function N(q), which is given by the integral,

$$N(q) = \frac{1}{4\pi}\int_{S_q} \sin\theta\,d\theta\,d\varphi \quad , \tag{4.1}$$

where S_q is the domain (φ,θ) for which, recalling Eq. (3.3), (see Fig. 4.1),

$$\frac{1}{|\sin\theta||\sin\varphi|} \leq q \quad . \tag{4.2}$$

Since φ,θ and q are related by Eq. (3.3), we can write

$$d\varphi = d\sin^{-1}(1/q\sin\theta) = \frac{-1/\sin\theta}{(1-(1/q\sin\theta)^2)^{\frac{1}{2}}}\left(\frac{-1}{q^2}\right)dq \quad , \tag{4.3}$$

and (4.2) becomes

$$N(q) = \frac{1}{4\pi}\int_1^q \frac{1}{q^2}\,dq\left[2\int_{\sin^{-1}(\frac{1}{q})}^{\pi/2} \frac{1}{(1-(1/q\sin\theta)^2)^{\frac{1}{2}}}\,\frac{d\theta}{\sin\theta}\right] . \tag{4.4}$$

Integrating (4.4) we obtain the function, shown in Fig. 4.2,

$$N(q) = 1 - \frac{1}{q}\ , \quad q \geq 1, \tag{4.5}$$

and the density distribution function turns out to be

$$\frac{dN(q)}{dq} = \frac{1}{q^2} \quad . \tag{4.6}$$

We proceed in a similar way to evaluate the cumulative probability function $N(\lambda)$,

$$N(\lambda) = \frac{1}{4\pi}\int_{S_\lambda} \sin\theta d\theta d\varphi \quad , \tag{4.7}$$

where S_λ is the domain (φ,θ) for which $\frac{1}{|\sin\varphi tg\theta|} \leq \lambda$ (Fig. 4.3). We obtain the cumulative probability function,

$$N(\lambda) = \frac{2}{\pi}\,tg^{-1}\lambda \quad , \quad \lambda \geq 0 \ , \tag{4.8}$$

plotted in Fig. 4.4.

The density distribution with respect to the width is consequently,

$$\frac{dN(\lambda)}{d\lambda} = \frac{2}{\pi}\,\frac{1}{1+\lambda^2} \quad . \tag{4.9}$$

5. Voltage Pulse Induced by a Rectilinear Track

The mathematical operation leading to the effective Green function corresponds simply to constructing the pulse for a given wire not only by means of the output of its amplifier, but adding in a summing amplifier the pulses of the amplifiers connected to the two adjacent wires with a weight of -0.3.

We shall now consider the induced voltage pulse obtained from the summing amplifiers associated with each sensing wire. We start from the knowledge of the above defined "input pulse" and from the voltage waveform induced by unit point charge starting at a distance h from the sensing wire in the y direction (Fig. 2.7) and at a given large distance above the screen grid. As defined in section 2, this induced voltage waveform is given by

$$\frac{1}{C}\,f(h,t) \quad , \tag{5.1}$$

where C is the capacitance of a wire and the associated input amplifier. Now we shall study the shape (through a shape parameter) and the area of the total voltage pulse induced by a charge track.

A track element, having direction θ,φ, and crossing the x axis in $\bar{x}$, will induce a voltage pulse

$$\frac{1}{C}\,f(h,t+\frac{h}{u}\,\frac{1}{|\sin\varphi tg\theta|})\,\frac{d}{|\sin\varphi\sin\theta|}\,dh \quad , \tag{5.2}$$

and the total voltage pulse induced by such a track will be

$$F(t) = \int_{-\infty}^{+\infty} \frac{1}{C}\,f(h,t+\frac{h}{u}\,\frac{1}{|\sin\varphi tg\theta|})\,\frac{d}{|\sin\varphi\sin\theta|}\,dh \ . \tag{5.3}$$

Recalling from Eqs. (3.4) and (3.3) the width T of the "input pulse" and its total charge Q_{2w}, we can write

$$F(t) = \frac{Q_{2w}}{2wC}\int_{-\infty}^{+\infty} f(h,\frac{Th}{2w}+t)\,dh \quad . \tag{5.4}$$

By symmetry considerations we have

$$f(h,t) = f(-h,t) = f(|h|,t) \quad , \tag{5.5}$$

so that Eq. (5.4) can be written

$$F(t) = \frac{Q_{2w}}{2wC}\int_{-\infty}^{+\infty} f(|h|,\frac{Th}{2w}+t)\,dh \quad . \tag{5.6}$$

From this we can state that the centroid of F(t) is independent of T, that is of the direction θ,φ of the track. The elementary contributions $f(|h|, Th/2w + t)dh$ in Eq. (5.6) can be associated in pairs at h and -h. These pairs represent two equal pulses, the one advanced in time by Th/2w, the other delayed by the same amount. Obviously, the centroid position of this pair is independent of the magnitude of these time displacements, and thus it is the true centroid of the whole pulse F(t) independent of T.

For convenience, we now redefine the f(h,t) so that the centroid of the whole F(t) be at t = 0.

We now calculate the rms width L of F(t),

$$L^2 = \frac{\int_{-\infty}^{+\infty} t^2F(t)dt}{\int_{-\infty}^{+\infty} F(t)dt} \ . \tag{5.7}$$

By using Eq. (5.6) and the Steiner theorem, Eq. (5.7) can be written in the form,

$$L^2 = \frac{\int_{-\infty}^{+\infty} dh\left[\int_{-\infty}^{+\infty} t^2f(|h|,t)dt + \int_{-\infty}^{+\infty} f(|h|,t)\,\frac{T^2h^2}{4w^2}\,dt\right]}{\int_{-\infty}^{+\infty} dt\int_{-\infty}^{+\infty} dh\,f(|h|,t)} \ . \tag{5.8}$$

Finally,

$$L^2 = L_o^2 + \frac{T^2\overline{h^2}}{4w^2} = L_o^2 + L_s^2 \quad , \tag{5.9}$$

where

$$\overline{h^2} = \frac{\int_{-\infty}^{+\infty} h^2 dh \int_{-\infty}^{+\infty} f(|h|,t)dt}{\int_{-\infty}^{+\infty} dh \int_{-\infty}^{+\infty} f(|h|,t)dt} \quad , \tag{5.10}$$

and

$$L_o^2 = \frac{\int_{-\infty}^{+\infty} dt\, t^2 \int_{-\infty}^{+\infty} f(|h|,t)dh}{\int_{-\infty}^{+\infty} dt \int_{-\infty}^{+\infty} f(|h|,t)dh} = \frac{\int_{-\infty}^{+\infty} t^2 F_o(t)dt}{\int_{-\infty}^{+\infty} F_o(t)dt} \quad . \tag{5.11}$$

L_o^2 is the quadratic width of the shortest pulse $F_o(t)$, arising from a track parallel to the screen grid plane and orthogonal to sensing wires ($\theta = \varphi = \pi/2$). Thus we have proved that the r.m.s. width of F(t) is determined by the usual rule of quadratic addition of the r.m.s. width T of the input pulse and the r.m.s. width L_o of the ionization chamber response $F_o(t)$.

We shall compare the results obtained by calculating the actual waveforms with an approximate reference pulse $f_r(h,t)$ of triangular shape of total width $T_D = 2G/u$, and its amplitude decreasing linearly from 1 to 0 when h spans the interval 0 to w (see Fig. 5.1) given by,

$$f_r(h,t) = (1-|\frac{h}{w}|)(1-|1-\frac{2t}{T_D}|) \quad , \quad -w \le h \le w, \quad 0 \le t \le T_D \quad . \tag{5.12}$$

We note that the width T_D is connected to the reference time T_r by,

$$\frac{T_r}{T_D} = \frac{w}{G} \quad . \tag{5.13}$$

We can relate the r.m.s. width L_o to the nominal width T_D of the reference pulse $f_r(h,t)$ with a dimensionless coefficient

$$T_D = \beta L_o \quad . \tag{5.14}$$

For the reference triangular pulse $\beta_r = \sqrt{24} = 4.898$, while for the calculated geometry and potentials (a), (b) of section 2, $F_o(t)$ is shown in Fig. 2.9 and in both cases $\beta = 4.02$. Similarly, we can relate the r.m.s. width L_s to the nominal width T of the input current pulse with a dimensionless coefficient writing

$$T = \xi L_s \quad . \tag{5.15}$$

Recalling Eq. (5.10),

$$\xi = \frac{2w}{\sqrt{\overline{h^2}}} \quad , \tag{5.16}$$

where $\sqrt{\overline{h^2}}$ is a measure of the resolution of the projection chamber in the y direction. For the reference pulse $f_r(h,t)$ $\xi_r = \sqrt{24} = 4.898$, while for the calculated f(h,t), in the case (a) $\xi = 3.6$ and in the case (b) $\xi = 3.8$. Equation (5.9) now becomes,

$$L^2 = \frac{T_D^2}{\beta^2} + \frac{T^2}{\xi^2} \quad . \tag{5.17}$$

The resolution in y direction using the "effective Green function" is shown in Fig. 5.2(a), where the partial contributions to the pulse on the considered sensing wire induced by equal charge elements starting at different distance h from it are plotted. In Fig. 5.2(b) the same distribution is plotted for comparison when using the true Green function. The great improvement in y resolution obtained with the effective Green function is apparent. It has been achieved, however, at the cost of reduction in pulse amplitude.

For the following discussion we shall need the area A of F(t),

$$A = \int_{-\infty}^{+\infty} F(t)dt = \frac{Q_{2w}}{Q_o} \int_{-\infty}^{+\infty} F_o(t)dt = \frac{Q_{2w}}{Q_o} A_o \quad . \tag{5.18}$$

The true area A_o can be related to the area $Q_o T_D/4C = A_{ro}$ of the global reference pulse $F_{ro}(t)$,

$$F_{ro}(t) = \frac{Q_o}{2wC} \int_{-w}^{+w} f_r(|h|,t)dh \quad , \tag{5.19}$$

by a dimensionless coefficient α,

$$\alpha = \frac{A_o}{A_{ro}} \quad . \tag{5.20}$$

Thus,

$$\alpha = \frac{2}{T_D w} \int_{-\infty}^{+\infty} dh \int_{-\infty}^{+\infty} f(|h|,t)dt \quad , \tag{5.21}$$

and, for calculated cases (a), (b) of Section 2,

$$\alpha = 0.36 \quad .$$

It turns out that as far as the induced pulse is concerned, the potential distributions of the cases (a) and (b) give nearly the same results. However, case (b) gives the advantage of recovering the initial geometry of the track by a defocusing effect of the first sensing grid neglecting the time distortion due to the electrons which have passed in low field zones near the saddle points.

Also, case (a) introduces delays in the electrons passing near the saddle point at the screen grid. Case (b) adds to this a delay due to the saddle point at the sensing grid. These effects are too small to be seen on the overall pulse but can be seen in the partial responses f(h,t) of Figs. 2.8(a) and (b). These effects are underestimated because in our calculations we have taken into account only the longer path of the electrons involved, while in reality the reduced velocity of the electrons not traveling always in the saturated region will also play a role.

6. Pulse Shaping Filters

In the preceding section we have recognized the centroid property of the voltage pulse F(t) as faithfully giving the x coordinate of the track segment corresponding to the y coordinate of the wire, independently of the track direction. We now search for a filter capable of determining the centroid of F(t).

Attention is focused here on sensing the presence of the pulse and on the timing, rather than on measuring very accurately its amplitude or area. The response g(t) of such a filter is,

$$g(t) = \frac{4}{T_M}\left(\frac{T_M}{2} - t\right)\left[1(t)-1(t-T_M)\right] \quad , \qquad (6.1)$$

and it is shown in Fig. 6.1. The filter, when driven by F(t), gives an output pulse

$$W(t) = \frac{4}{T_M}\int_{-\infty}^{+\infty}\left(\frac{T_M}{2} - t + \tau\right)\left[1(t-\tau)-1(t-\tau-T_M)\right]F(\tau)d\tau \quad . \qquad (6.2)$$

The pulse W(t) crosses the zero line at a time t_o (for which $W(t_o) = 0$), determined by,

$$\left(t_o - \frac{T_M}{2}\right)\int_{t_o-T_M}^{t_o} F(\tau)d\tau = \int_{t_o-T_M}^{t_o} \tau\, F(\tau)d\tau \quad . \qquad (6.3)$$

Solving for t_o we have

$$t_o = \frac{T_M}{2} + \frac{\int_{t_o-T_M}^{t_o} \tau\, F(\tau)d\tau}{\int_{t_o-T_M}^{t_o} F(\tau)d\tau} \quad , \qquad (6.4)$$

$$t_o = \frac{T_M}{2} + t_c \quad , \qquad (6.5)$$

where t_c is the centroid of F(t), provided that F(t) is zero before $t_o - T_M/2$ and after $t_o + T_M/2$. A zero crossing detection of W(t) gives, therefore, a measurement of the centroid of F(t) assuming the above restrictions on the width of F(t) are satisfied.

The zero crossing slope S of W(t) is $4A/T_M$ if A [volt sec] is the area of F(t). This slope is independent of the shape of F(t) as every element F(t) dt = dA of the exciting pulse gives (because of the linear shape of g(t) a contribution to the total slope $4/T_M$ dA, irrespective of the position of dA. In Fig. 6.3 the normalized zero crossing slope is shown. It is also given for pulses of width larger than T_M for which the preceding considerations are not valid, but for which the filter does not give any timing error if F(t) is symmetrical with respect to its centroid.

This shape-dependent slope is calculated with pulses $F_r(t)$ at the input of the considered filter. $F_r(t)$ is obtained by superposing the voltage contributions

$$\frac{Q_{2w}}{2Cw}\, f_r(h,t)\, dh \qquad (6.6)$$

suitably shifted in time, according to the length T of the "input current pulse" which is related to the track direction.

$$F_r(t) = \frac{4A_r}{T_D T}\int_{-T/2}^{T/2}\left(1-\left|\frac{\tau}{T/2}\right|\right)\left(1-\left|1 - \frac{t+\tau}{T_D/2}\right|\right) \cdot \left\{1(t+\tau)-1(t+\tau-T_D)\right\} d\tau \quad , \qquad (6.7)$$

where $\frac{Q_{2w}}{C} = 4\frac{A_r}{T_D}$.

$F_r(t)$ turns out to be the convolution of two triangular waveforms of width T and T_D, respectively. The resulting pulses are shown in Fig. 6.2, and can be compared with the F(t) shown in Figs. 2.9(a) and (b).

The filter output $W_{1r}(t)$ is given by the $\mathcal{L}^{-1}$ transform of the product of the $\mathcal{L}$ transform of $F_r(t)$ and the filter transfer function $H_1(s)$, which are respectively,

$$\mathcal{L}(F_r(t)) = \frac{64A_r}{T^2T_D^2}\,\frac{e^{-s\frac{T_D}{2}}}{s^4}\left(\cosh\frac{sT_D}{2} -1\right)\left(\cosh\frac{sT}{2} -1\right) \quad , \qquad (6.8)$$

and

$$H_1(s) = \frac{4}{6}\cosh\frac{sT_M}{2} - \frac{8}{T_M s^2}\sinh\frac{sT_M}{2} \quad . \qquad (6.9)$$

In Fig. 6.4, the calculated voltage waveform $W_{1r}(t)$ is shown for $T_M/T_D = 1$ and shifted in time so that the zero crossing point is at t = 0.

Let us now calculate the amplifier output noise. The time scale of the filter response is in the range of a few microseconds. Thus, only the series noise needs to be considered. The mean square noise voltage referred to the input is

$$e_{1N}^2 = \frac{e_n^2}{2}\int_{-T_M/2}^{T_M/2}\left(\frac{4t}{T_M}\right)^2 dt = \frac{e_n^2}{2}\cdot\frac{4}{3}T_M \quad . \qquad (6.10)$$

The timing variance is given by the square of the ratio of the r.m.s. noise and the signal slope at zero crossing,

$$e_{1t}^2 = \frac{e_{1N}^2}{S^2} = \frac{e_n^2}{2}\,\frac{1}{12}\,\frac{T_M^3}{A^2} \quad , \qquad (6.11)$$

if $T + T_D < T_M$. When this last condition is not satisfied

$$e_{1t}^2 = \frac{e_n^2}{2}\,\frac{T_M^3}{12}\,\frac{1}{A^2 n_1^2\left(\frac{T_M}{T_D}, \frac{T}{T_D}\right)} \quad , \qquad (6.12)$$

where n_1 is the normalized slope plotted in Fig. 6.3.

Let us now evaluate the noise to signal ratio given by this filter in order to recognize the presence of

a track. The normalized peak amplitude m_1 as a function of the parameters T_M/T_D and T/T_D of the calculated $W_{1r}(t)$ is plotted in Fig. 6.5.

The noise to signal ratio squared Z_1^2 can be written

$$Z_1^2 = \frac{e_n^2}{2}\,\frac{T_M}{12}\,\frac{1}{A^2 m_1^2(\frac{T_M}{T_D}, \frac{T}{T_D})} \quad . \qquad (6.13)$$

We will now investigate the behavior of another bipolar filter which does not produce any ballistic deficit for short "input pulses", that is when $T < T_M/2 - T_D$ and would be the optimum filter for a triangular pulse of width T_M at its input. The filter considered has a bipolar rectangular response as shown in Fig. 6.6. This filter does not introduce systematic zero crossing timing errors if the input pulses are symmetrical. In Fig. 6.7, the calculated voltage waveforms $W_{2r}(t)$ for $T_M/T_D = 1.5$ are shown.

The mean square noise referred to the input is, in this case,

$$e_{2N}^2 = \frac{e_n^2}{2}\,T_M \quad . \qquad (6.14)$$

In Fig. 6.8 the normalized slope n_2 is shown. In Fig. 6.9 the normalized peak amplitude m_2 is given. The reference slope $4\sqrt{3}/2\ A/T_M$ and the reference amplitude $4\sqrt{3}/2\ A$ have been chosen in order to be able to compare the performance of the two filters by simply comparing the n_1 and m_1 values with the corresponding n_2 and m_2 values.

It should be noted that n_2 increases when T becomes smaller even in the region $T < T_M - T_D$, while n_1 remains constant, in this region. For this filter, the timing variance is

$$e_{2t}^2 = \frac{e_n^2}{2}\,\frac{T_M^3}{12}\,\frac{1}{A^2 n_2^2(\frac{T_M}{T_D}, \frac{T}{T_D})} \quad , \qquad (6.15)$$

and the noise to signal ratio squared

$$Z_2^2 = \frac{e_n^2}{2}\,\frac{T_M}{12}\,\frac{1}{A^2 m_2^2(\frac{T_M}{T_D}, \frac{T}{T_D})} \quad . \qquad (6.16)$$

Equations (6.15) and (6.16) are formally identical to Eqs. (6.12) and (6.13), respectively. In formulas (6.12), (6.13), (6.15), (6.16), T_D should be substituted by $\beta_r/\beta\ T_D$ and T by $\xi_r/\xi\ T$ in order to approximate better the true pulses with the reference ones. However, as a first order approach, only calculations and design with the reference values will be dealt with.

We note that both filters are able to perform the timing correctly on the tracks which generate input pulses having width T much larger than T_D. In fact, the reference pulse at the input of the considered filter is the convolution of a triangular waveform of the fixed width T_D with a triangular waveform of width T, Eq. (6.7). When $T \gg T_D$, the reference pulse becomes again a triangular waveform. Then, both bipolar filters acting as differentiators give as their output a nearly bipolar rectangular waveform, where the zero crossing gives the correct timing of the track.

7. Design Guidelines and Discussion of the Results

Consider the expressions (6.12) or (6.15) and substitute for A the expression

$$A = \frac{Q_o T_D \alpha}{|\sin\theta|\,4C} = \frac{wdT_D\alpha}{|\sin\theta|\,2C} \quad ,$$

as given by Eqs. (5.18), (5.20), and (3.3) and assuming $\varphi = 90^\circ$, that is the worst case as far as the timing resolution is concerned. We obtain for the timing variance,

$$e_t^2 = \frac{e_n^2}{2}\,\frac{T_D}{12}\,(\frac{T_M}{T_D})^3\,\frac{4C^2}{\alpha^2}\,\frac{1}{w^2d^2}\,\frac{\sin^2\theta}{n^2(\frac{T_M}{T_D}, \frac{T}{T_D})} \quad . \qquad (7.1)$$

By substituting Eq. (3.4),

$$e_t^2 = \frac{e_n^2}{2}\,\frac{T_D}{12}\,(\frac{T_M}{T_D})^3\,\frac{4C^2}{\alpha^2}\,\frac{1}{w^2d^2}\,\frac{1}{\lambda^2}\,\frac{\cos^2(\tan^{-1}1/\lambda)}{n^2} \quad . \qquad (7.2)$$

Similarly, from Eqs. (6.13) and (6.16), we obtain for the amplitude variance (noise to signal ratio squared) at the output of the timing filter,

$$Z^2 = \frac{e_n^2}{12}\,\frac{1}{12T_D}\,\frac{4C^2}{\alpha^2 w^2 d^2}\,\frac{T_M}{T_D}\,\frac{1}{\lambda^2}\,\frac{\cos^2(\tan^{-1}1/\lambda)}{m^2} \quad . \qquad (7.3)$$

Relationships (7.2) and (7.3) are our main design formulas. We assume: $e_n^2 = 3.10^{-18}$ volt^2/Hz (for an FET at room temperature); C = 20 pF, (10 pF for the input FET and 10 pF for the sensing wire capacitance plus stray capacitance); $d = 1.28 \times 10^{-12}$ Coulomb/m (8000 ion pairs/mm); $w = 10^{-3}$m (thus assigning an order of magnitude for the resolution in y direction);

$$T_r = \frac{2w}{u} = 0.4\ \mu s;$$

$$\alpha = 0.36;$$

$$\frac{T_M}{T_D} = 1,\ 1.5,\ 2 \text{ (tentative values).}$$

As it is necessary to recognize the presence of the pulses in order to be able to time them, T_D will be calculated from Eq. (7.3). We assume the maximum permissible noise to signal ratio squared so that the smallest pulses ($T = 0$, $\varphi = \pi/2$) can be unambiguously detected. We choose $Z^2 = 2 \times 10^{-2}$, which means that the signal amplitude is about seven times larger than r.m.s. noise. The pertinent m $(T_M/T_D, 0)$ values are determined from Figs. 6.5 and 6.9 for the two filters.

The resulting design parameters are shown in Table I for the first filter and in Table II for the second one.

The T_D values and the consequent gap dimension G preclude recognition and timing of multiple tracks separated by less than several millimeters in all considered cases in absence of more elaborate pulse processing. The space resolution $\mathcal{E}_x = u\,\mathcal{E}_t$ for the two filters is plotted as a function of $\lambda = T/T_r$ in Figs. 7.1 and 7.2.

The (amplitude) signal to noise ratio 1/Z for the two filters is plotted in Figs. 7.3 and 7.4 as a function of $\lambda = T/T_r$.

From these data a good choice appears to be filter 2 with $T_M/T_D = 1.5$, as it insures a spatial r.m.s. resolution $\mathcal{E}_x$ of 0.16 to 0.22 mm in the range $\lambda = 0$ to 10, with a total pulse width of 2.53 μsec for tracks parallel to the grid plane.

Another equally favorable choice would be filter 1 with $T_M/T_D = 1$, spatial r.m.s. resolution $\mathcal{E}_x = 0.17$ to 0.23 mm in the range $\lambda = 0$ to 10, with a total pulse width of 2.38 μsec for tracks parallel to the grid plane. The range of λ (calculated for the worst case of $\varphi = 90^\circ$) insures an accurate timing for more than 94% of the tracks in the isotropic case.

Furthermore, a calculation of $\mathcal{E}_x$ and 1/Z by using the true pulses F(t) from Figs. 2.9(a) and (b), instead of the reference ones $F_r(t)$ shown in Fig. 6.2, would give better timing resolution and higher signal amplitude to noise ratios, for tracks not parallel to the grid plane. This is due to the unexpected narrowing of the F(t) peaks with increasing λ. This arises due to the peculiar shape of the f(y,t) waveforms (negative minimum and two positive maxima) for a part of the range of y values (Figs. 2.8(a) and 2.8(b)). With a choice of a small value for T_M/T_D ($\approx$ unity), filter 1 no longer provides an accurate centroid measurement independently of the signal waveform. As it has been noted earlier in the paper, the centroid measurement is independent of the signal waveform only for pulses shorter than T_M. The two filters are, therefore, equivalent in this respect, and correct timing depends on the quasi symmetrical waveform of the input pulses for both filters. The condition of waveform symmetry is satisfied in practice as it is apparent from Figs. 29(a) and (b).

The filters derived here are optimized for timing measurements as required to achieve the best position resolution. Thus, they do not give the maximum possible signal to noise ratio for amplitude measurements. However, the resulting signal to noise ratio for amplitude measurements (Figs. 7.3 and 7.4) is sufficient for ionization loss (dE/dx) measurements, when this is required for particle identification. If this were not the case, a separate filter optimized for amplitude measurements would be necessary.

8. Preamplifier Considerations

In order to avoid crosstalk between the wires, the use of charge amplifiers providing a "virtual ground" at the input of the sensing wires seems compulsory.

The pulses called in this analysis "voltage pulses at the wires" will be, in reality, the voltage pulses at the output of the integrating preamplifiers. As mentioned in Section 2, electrostatic calculations provide the capacitance values reported in Fig. 8.1. The noise induced on a sensing wire by neighboring ones connected to their respective preamplifier virtual ground inputs is negligible. The weighted contribution of the two neighboring amplifiers used to obtain the required y resolution is equivalent to an increase of 9% of the input noise e_n.

9. Acknowledgements

The authors are grateful to W. J. Willis, R. L. Chase, and J. Fischer for many fruitful discussions. E. Gatti thanks for the hospitality in the stimulating environment of the Brookhaven National Laboratory.

References

1. G. Charpak, D. Rahm, and H. Steiner; Nucl. Instr. & Meth. 80, 13(1970).

2. D. Nygren; 1974 PEP Summer Study (PEP 137).

3. C. Rubbia; EP Internal Report 77-8, CERN, 16 May (1977).

4. H. H. Chen, J. F. Lathrop, and J. Learned; "Further Observation of Ionization Electrons Drifting in Liquid Argon". IEEE Trans. Nucl. Sci., Feb. (1978).

5. J. C. Maxwell; "Electricity and Magnetism". III Ed., Vol. 1, Section 203 - Cambridge, London, (1904).

6. K. R. Spangenberg; "Vacuum Tubes". P. 126, McGraw-Hill, (1948).

7. L. D. Landau and E. M. Lifshitz; "Electrodynamics of Continuous Media". Pergamon Press, Oxford (1960).

TABLE I

T_M/T_D	T_{D1} [μs]	T_{M1} [μs]	$(G/w)_1 = (T_D/T_r)_1$	ℓ_{x1} [mm]	$(T_M+T_D)_1$ [μs]
1	1.189	1.189	2.972	.167	2.38
1.5	1.006	1.509	2.515	.282	2.515
2	.993	1.986	2.48	.432	2.98

TABLE II

T_M/T_D	T_{D2} [μs]	T_{M2} [μs]	$(G/w)_2 = (T_D/T_r)_2$	ℓ_{x2} [mm]	$(T_M+T_D)_2$ [μs]
1	1.277	1.277	3.192	.152	2.554
1.5	1.013	1.519	2.53	.166	2.532
2	1.136	2.272	2.84	.2037	3.408

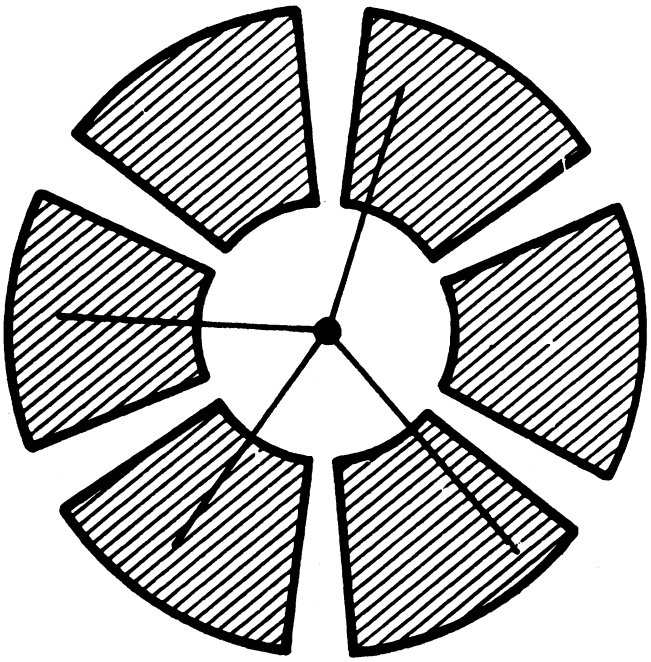

Fig. 1.1. Array of circular sectors as ambiguity resolver anodes for events with several prongs.

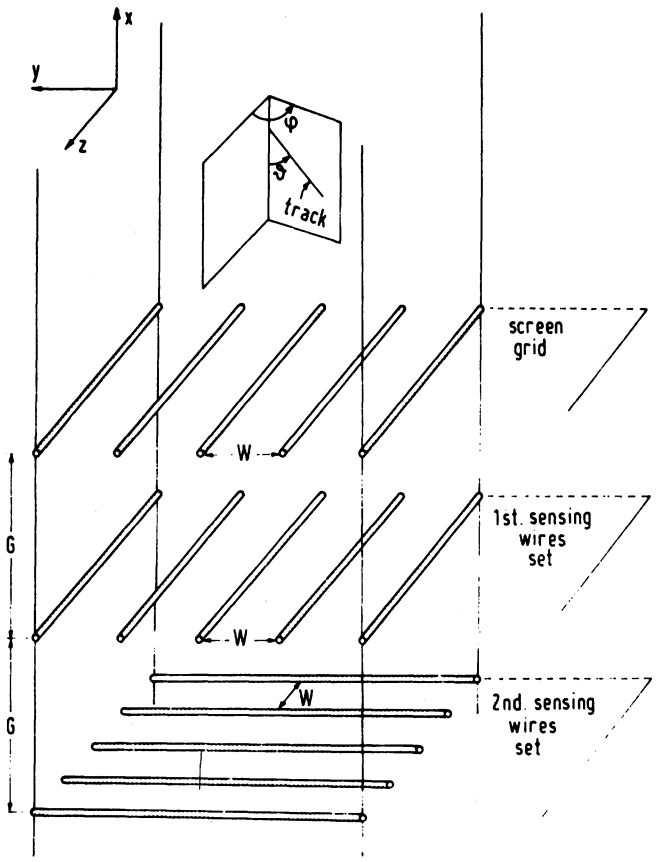

Fig. 1.2. Geometry of the grids and the reference frame.

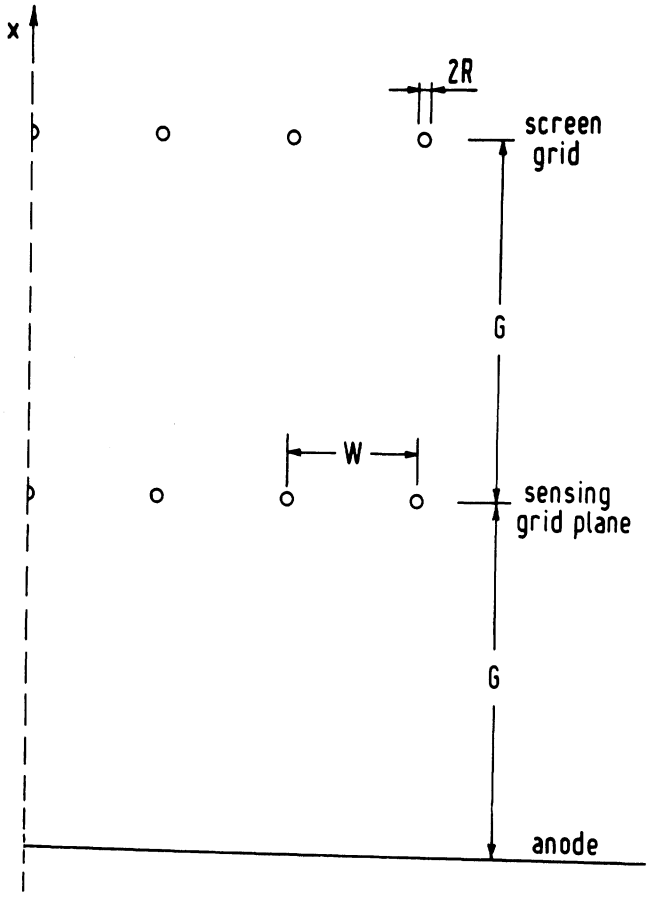

Fig. 2.1. Idealized geometry for a truncated chamber having only one sensing grid.

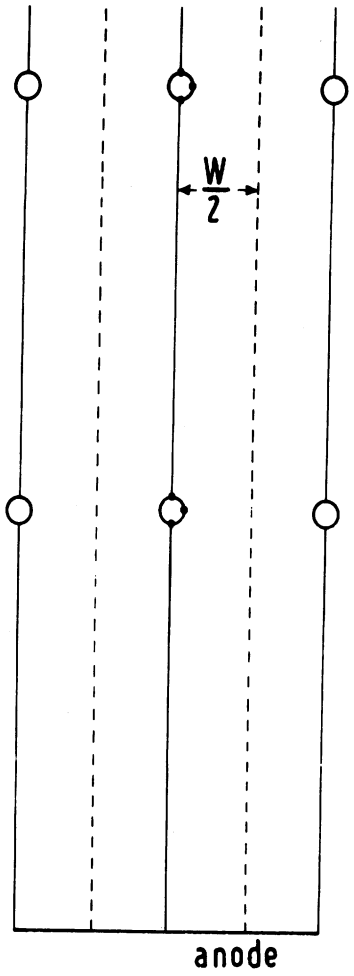

Fig. 2.2. Map of points at which the potential is imposed in order to calculate the influence coefficients and consequently the equipotential surfaces and field lines.

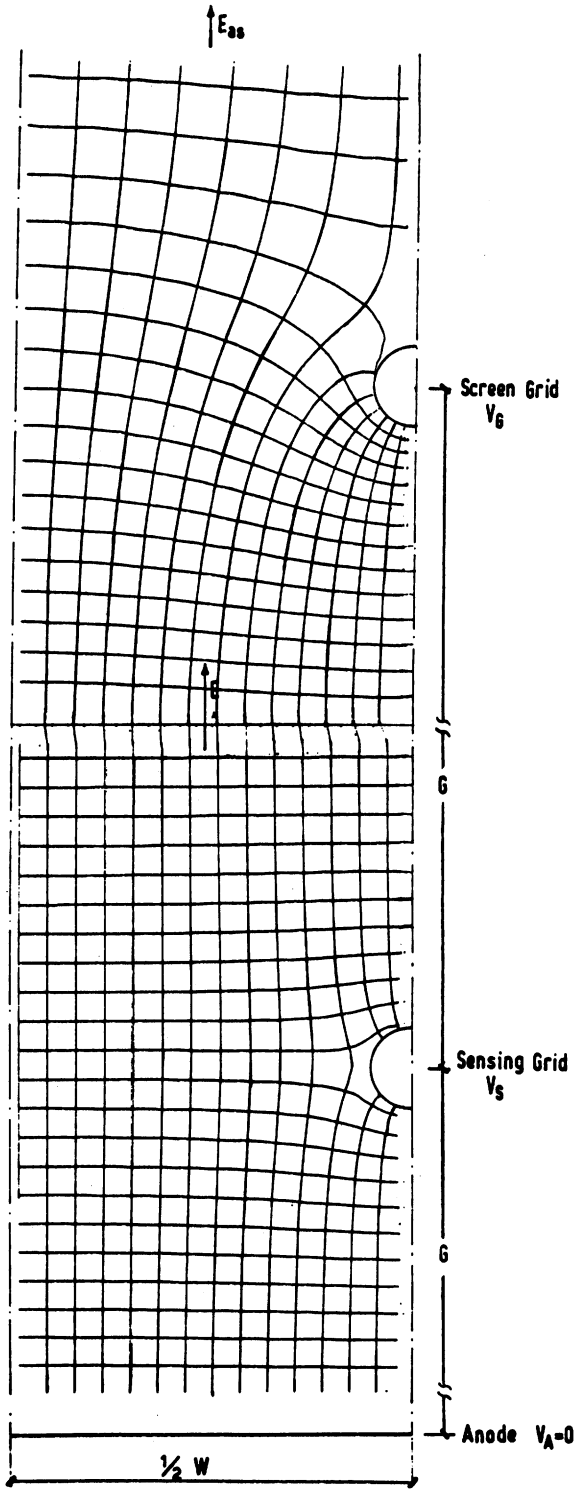

Fig. 2.3. Equipotential and field lines for the first set (a) of potentials (sensing grid at geometrical potential), calculated with the following parameter values: G = 2.66 mm, R = 0.05 mm, W = 1 mm, V_A/E_{as} G = 0, V_S/E_{as} G = 2 and V_G/E_{as} G = 4. The G/W ratio has been chosen near the design value suggested by Tables I and II.

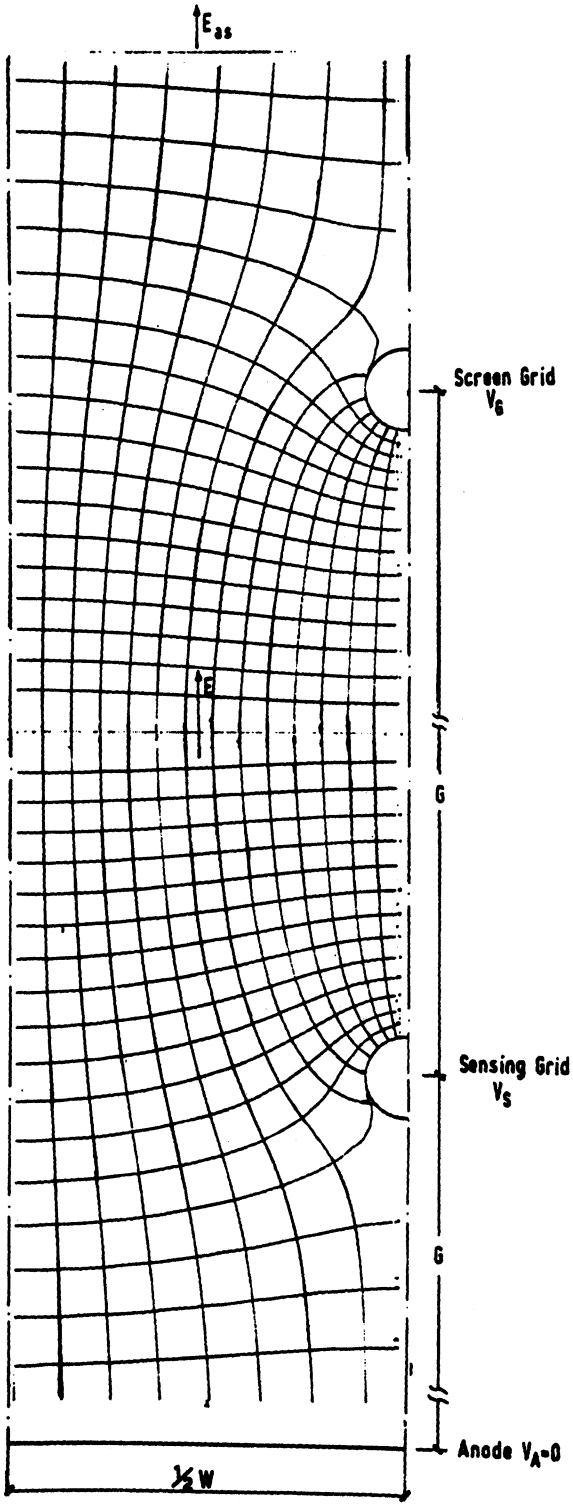

Fig. 2.4. Equipotential and stream lines for the second set (b) of potentials ("defocusing" sensing grid), calculated with the following parameter values G = 2.66 mm, R = 0.05 mm, W = 1 mm, V_A/E_{as} G = 0, V_S/E_{as} G = 1 and V_G/E_{as} G = 3.06. The G/W ratio has been chosen near the design value suggested by Tables I and II.

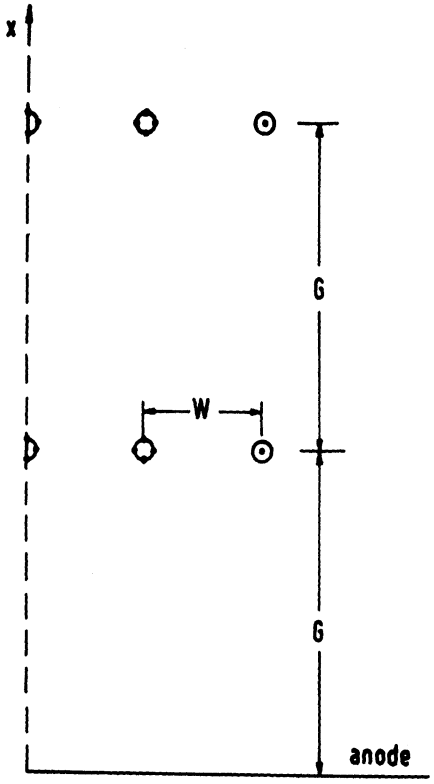

Fig. 2.5. Map of points at which the potential is imposed in order to calculate the influence coefficients in the Green function expression.

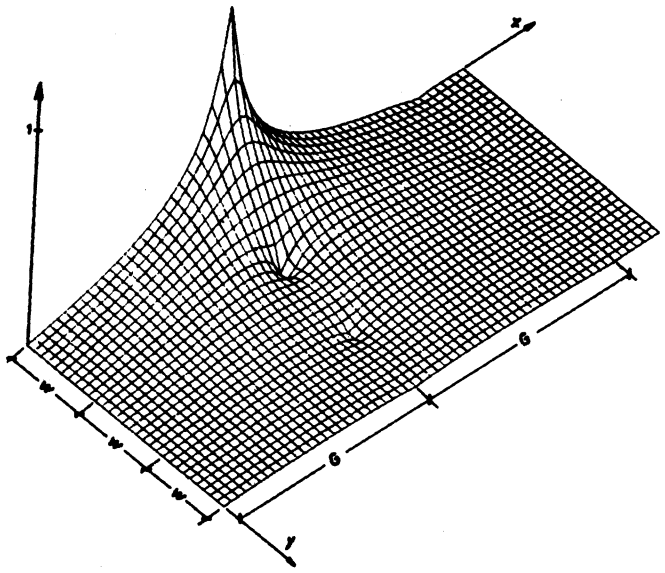

Fig. 2.6a$_1$ Green weighting function for a sensing wire: overall isometric representation. Calculated with the following parameter values: G = 2.66 mm, R = 0.05 mm and W = 1 mm.

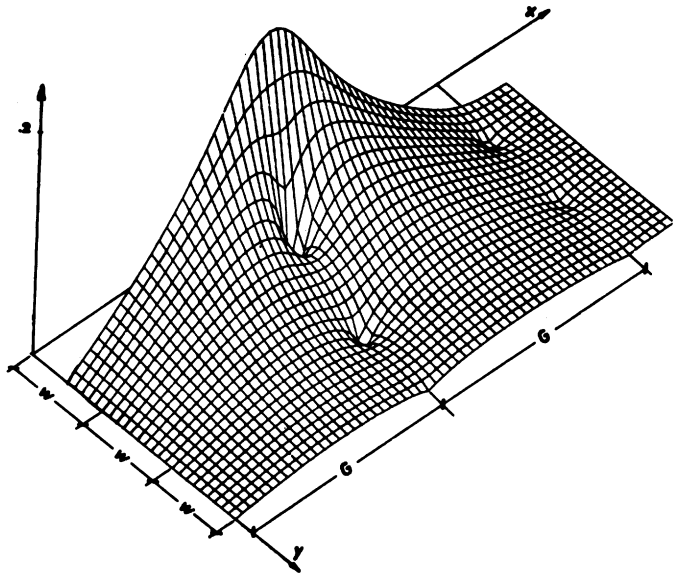

Fig. 2.6a$_2$ Green weighting function for a sensing wire: enlarged detail. Calculated with the following parameter values: G = 2.66 mm, R = 0.05 mm and W = 1 mm.

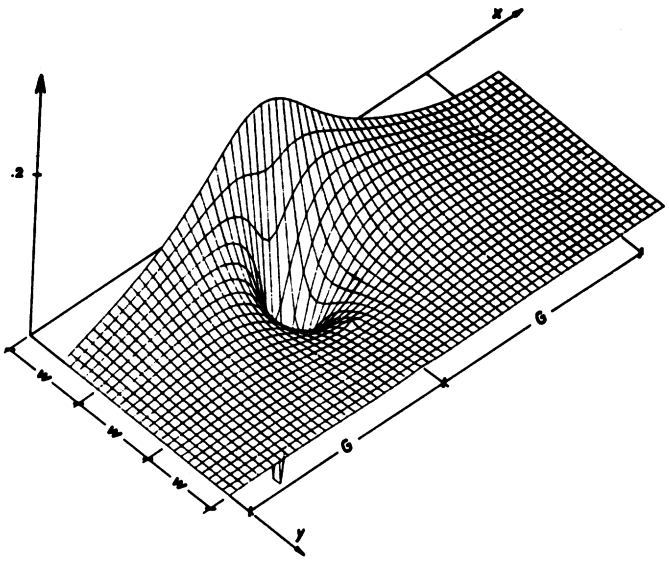

Fig. 2.6b$_2$ "Effective" Green function: enlarged detail. Calculated with the following parameter values: G = 2.66 mm, R = 0.05 mm, and W = 1 mm.

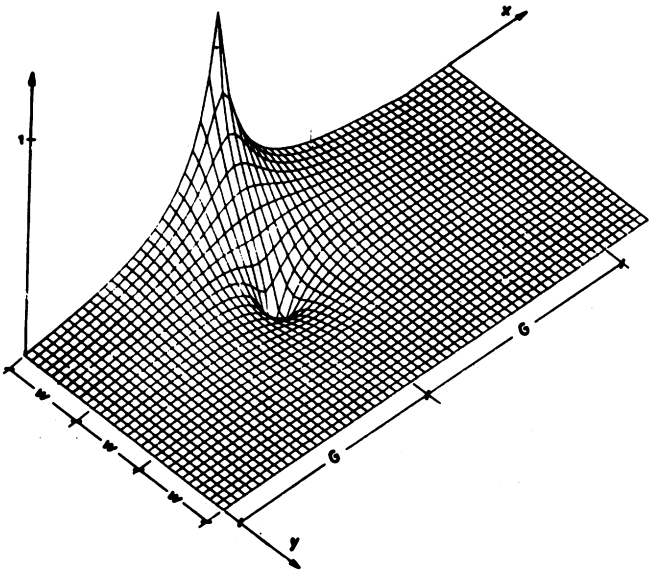

Fig. 2.6b$_1$ "Effective" Green function: overall isometric representation. Calculated with the following parameter values: G = 2.66 mm, R = 0.05 mm and W = 1 mm.

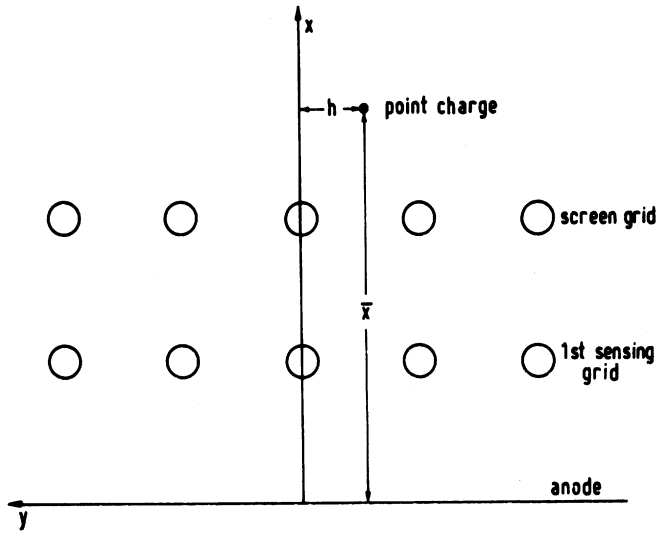

Fig. 2.7. Starting point of probe charge for the definition of f(h,t).

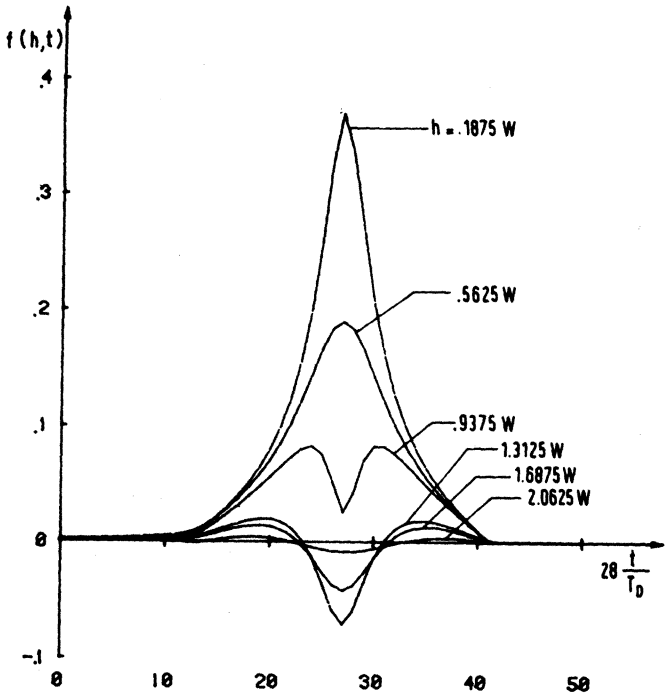

Fig. 2.8a.

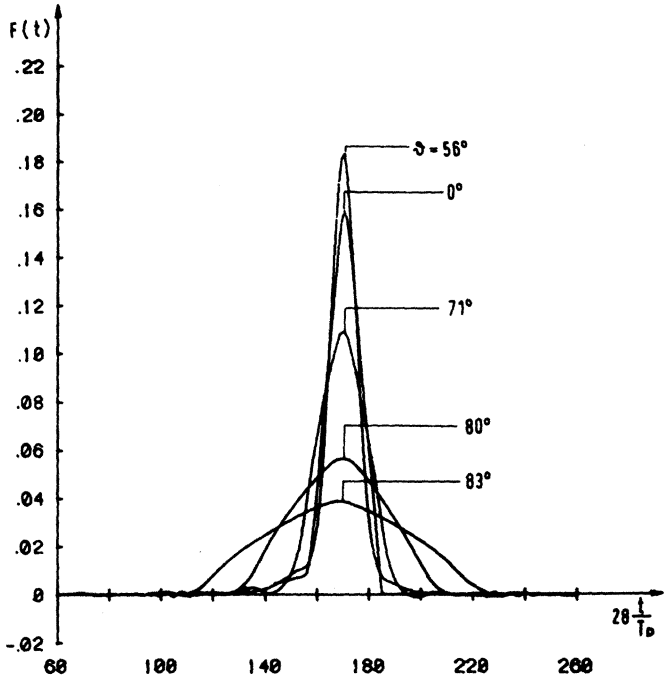

Fig. 2.9a.

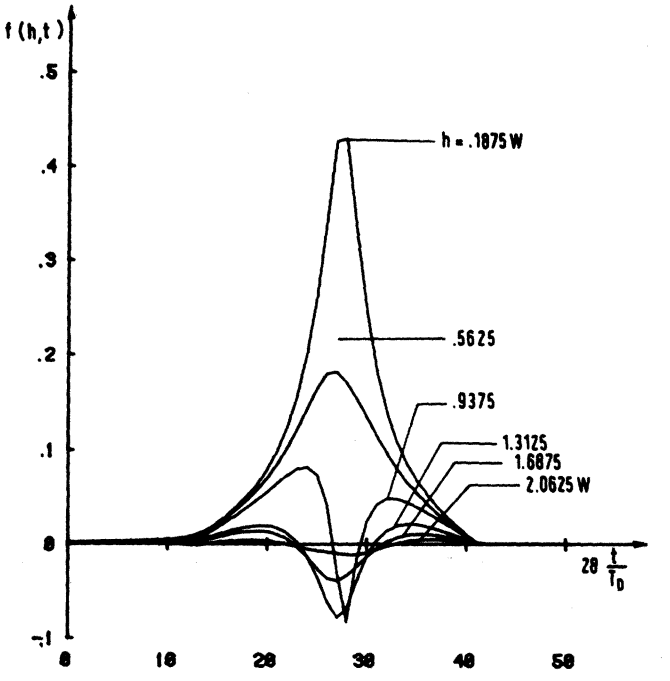

Fig. 2.8b. Induced charge waveform as calculated with the effective Green function for the first (a) and the second (b) set of electrode's potentials.

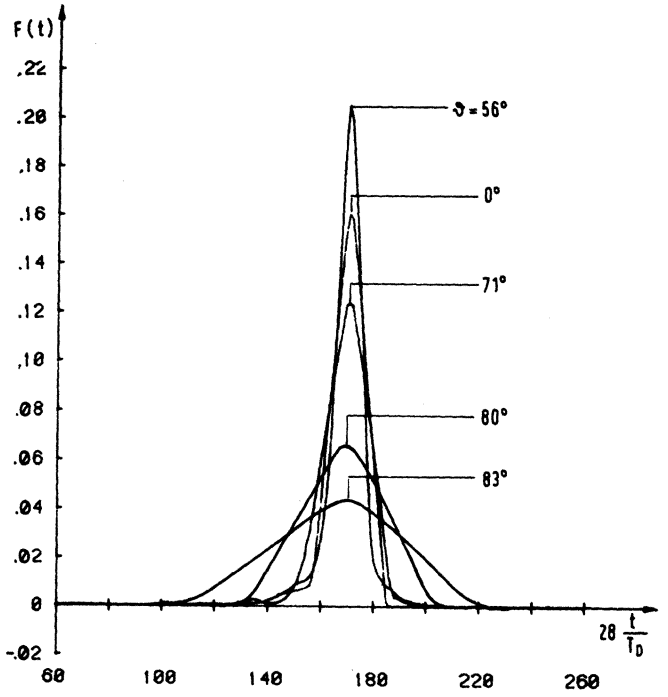

Fig. 2.9b. Induced charge pulse due to tracks having different angle θ (and φ = 90°) for the first set (a) and the second (b) set of electrode's potentials.

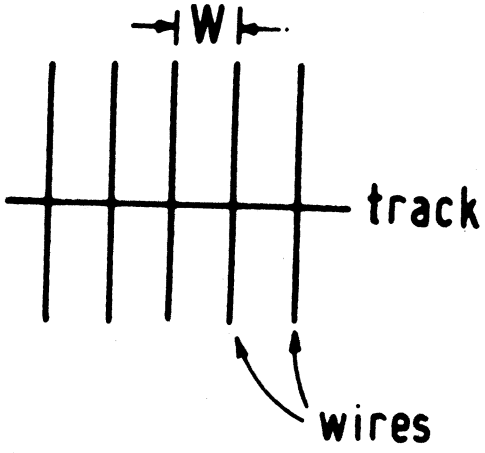

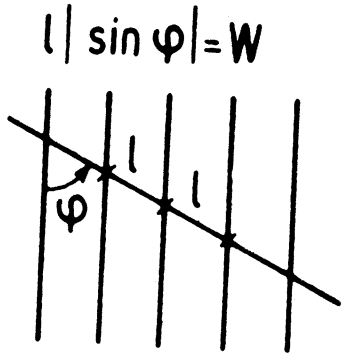

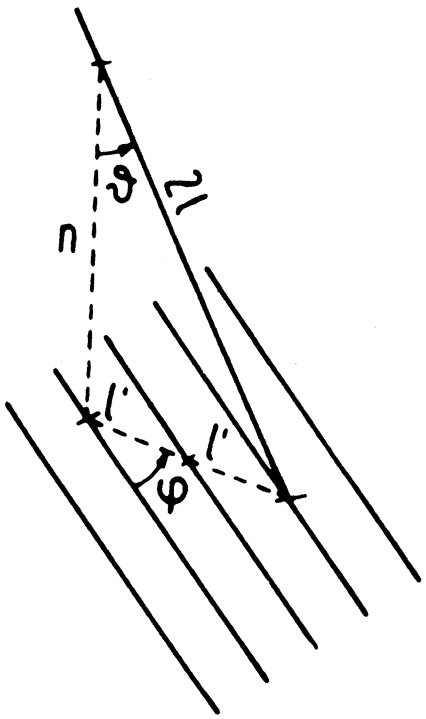

Fig. 3.1,2,3. Geometry of tracks with respect to grid wires.

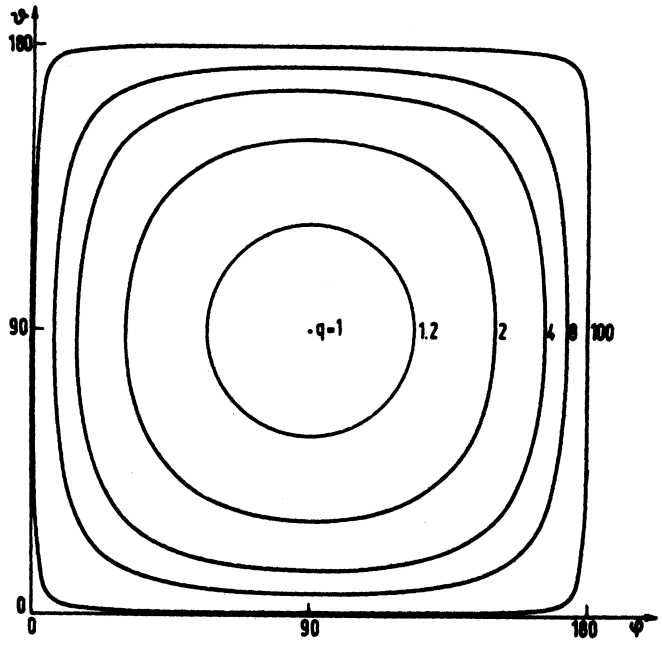

Fig. 4.1. Loci of constant charge "input pulses" in the plane φ, θ.

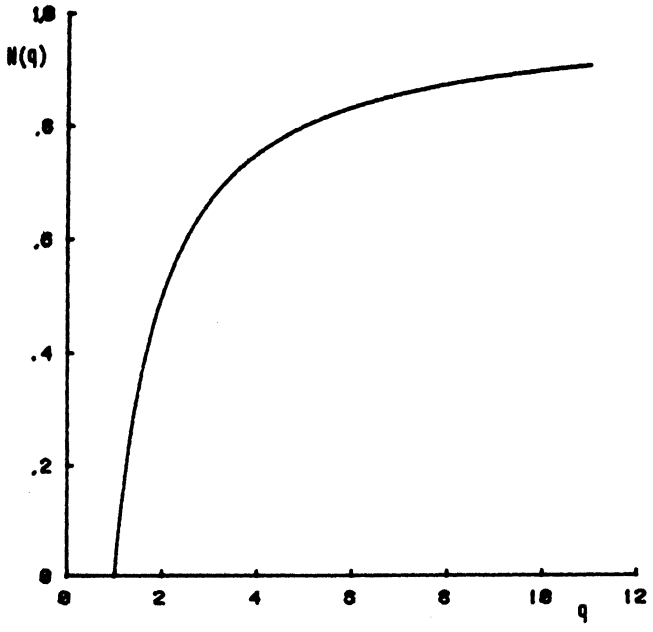

Fig. 4.2. Cumulative probability function N(q).

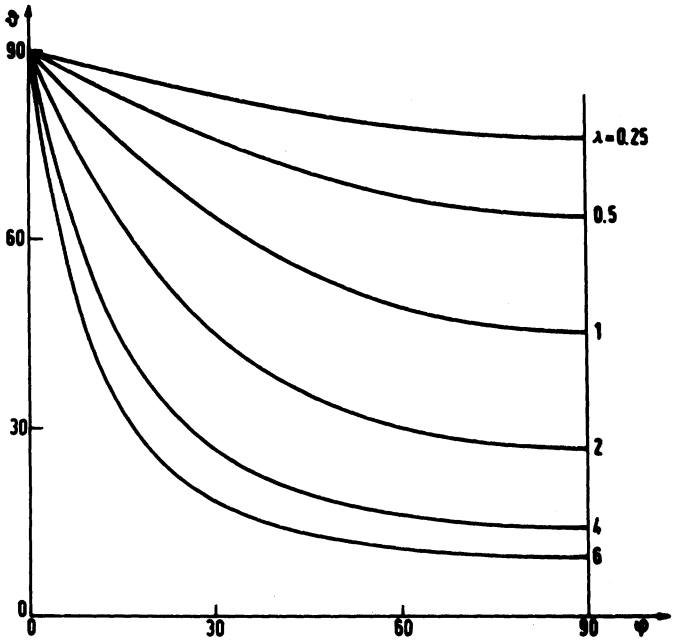

Fig. 4.3. Loci of constant width λ "input pulses" in the plane ω, θ; $\lambda = T/T_r$.

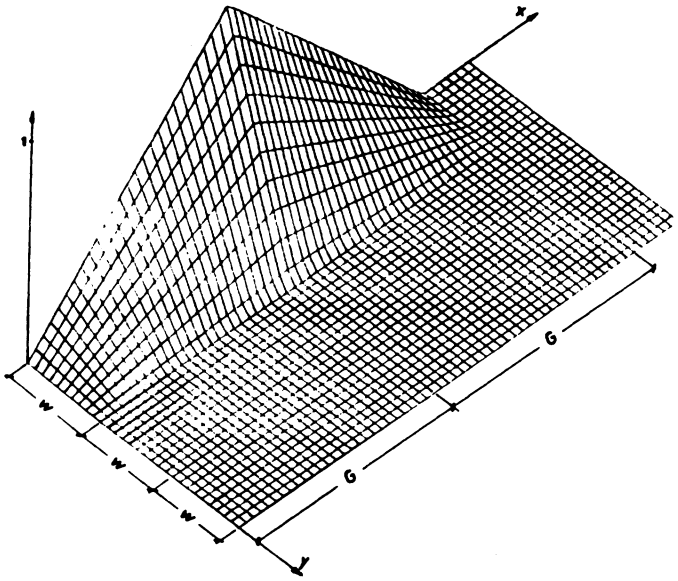

Fig. 5.1. Reference weighting function.

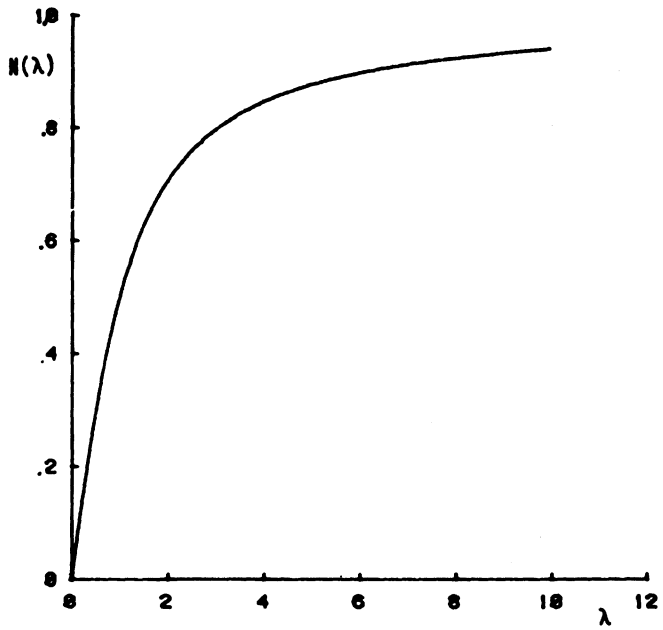

Fig. 4.4. Cumulative probability function N(λ).

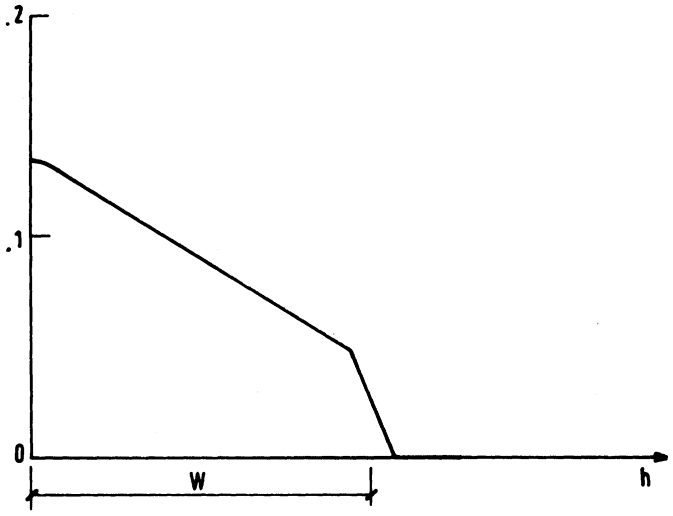

Fig. 5.2.a. Area of f(h,t) pulse as a function of h, for set (a) of electrode's potentials, giving an estimate of spatial resolution in y direction when using the "effective Green function" (a similar curve is obtained for set (b) of electrode's potentials).

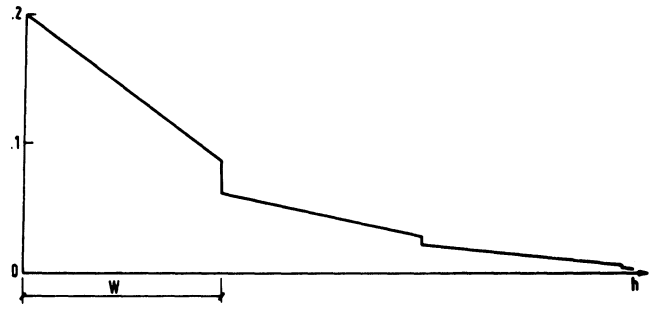

Fig. 5.2b. Same as for Fig. 5.2a, but using the "true" Green function.

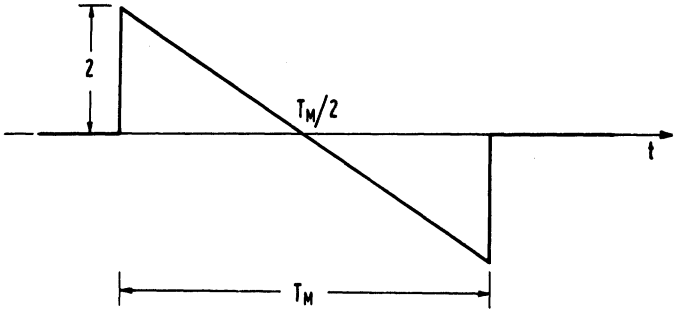

Fig. 6.1. δ-response of the first filter.

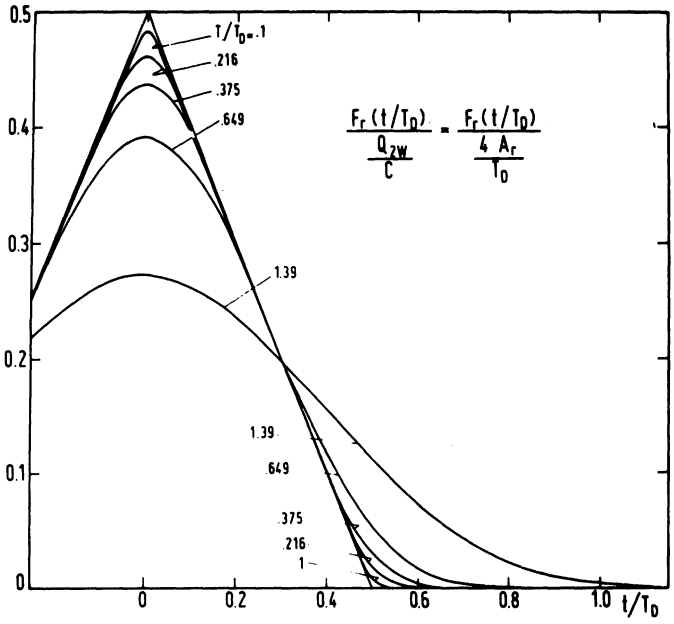

Fig. 6.2. Normalized reference pulses $F_r(t)$ generated by "input current pulses" of increasing length T.

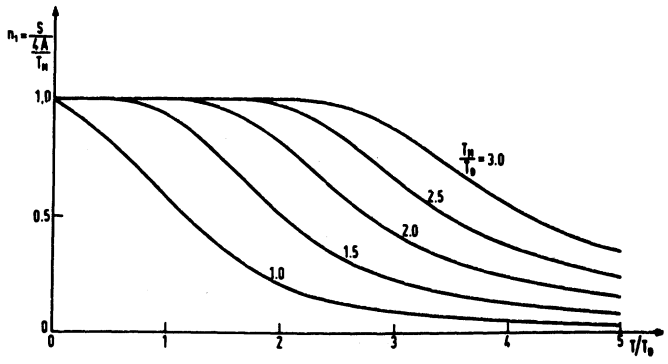

Fig. 6.3. Normalized zero crossing slope n_1 calculated for the voltage filter output $W_{1r}(t)$ (Fig. 6.4), with $F_r(t)$ as input pulses.

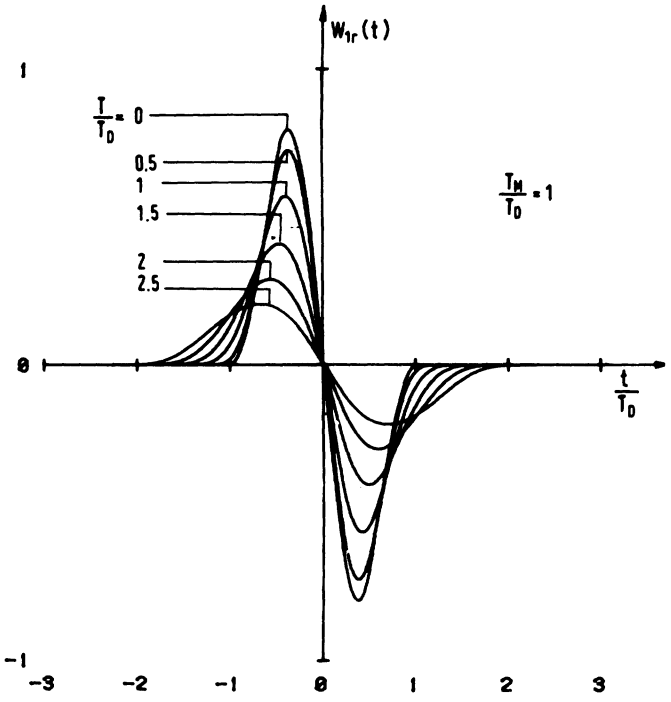

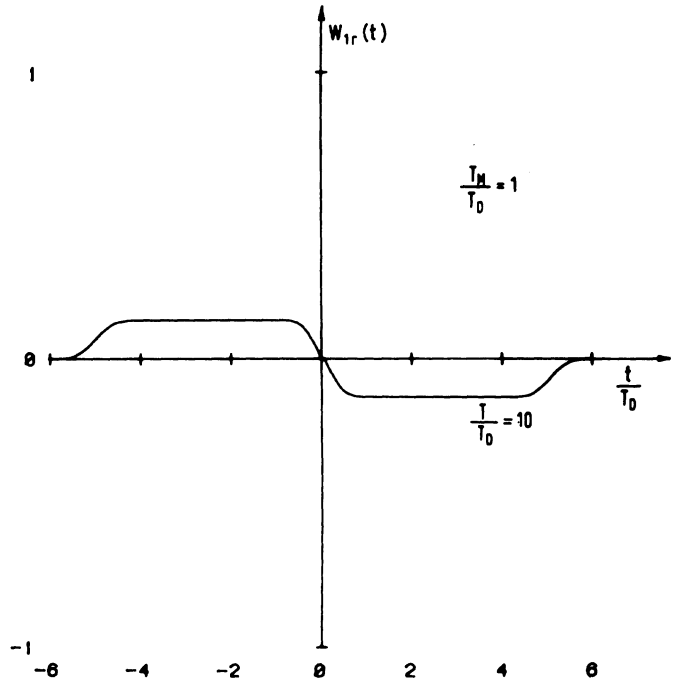

Fig. 6.4. Calculated filter output $W_{1r}(t)$ for $T_M/T_D = 1$ and for several T/T_D values.

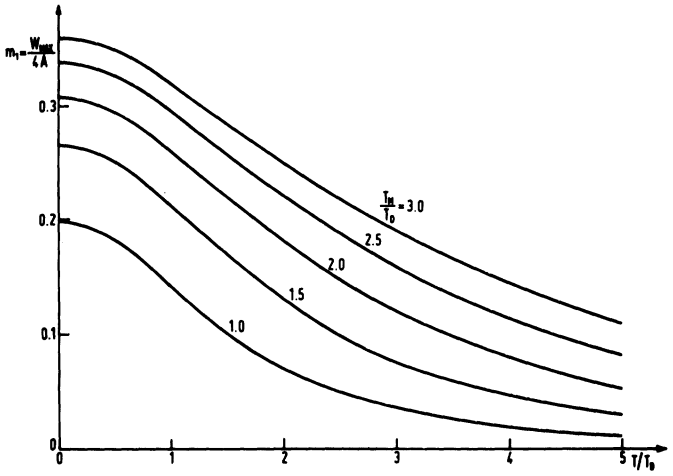

Fig. 6.5. Normalized peak amplitude m_1 of the voltage filter output $W_{1r}(t)$ (Fig. 6.4), with $F_r(t)$ as input pulses.

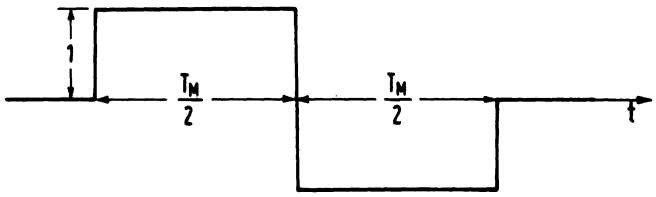

Fig. 6.6. δ-response of the second filter.

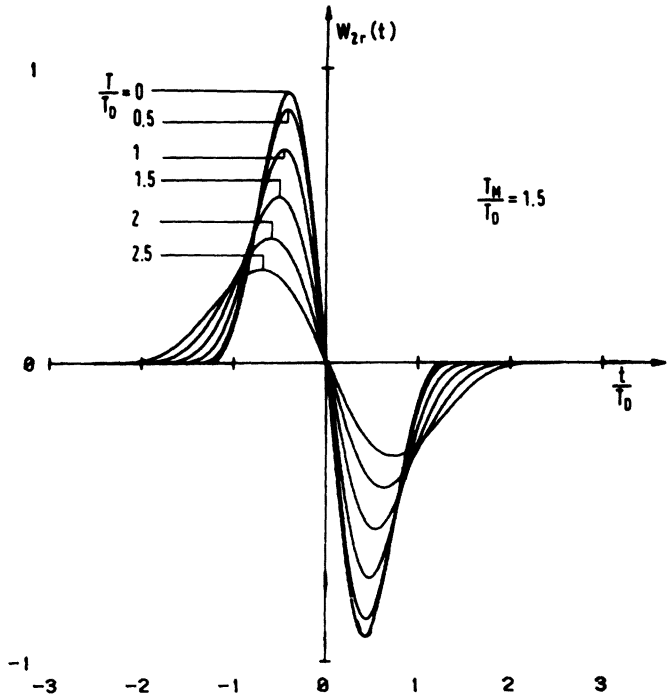

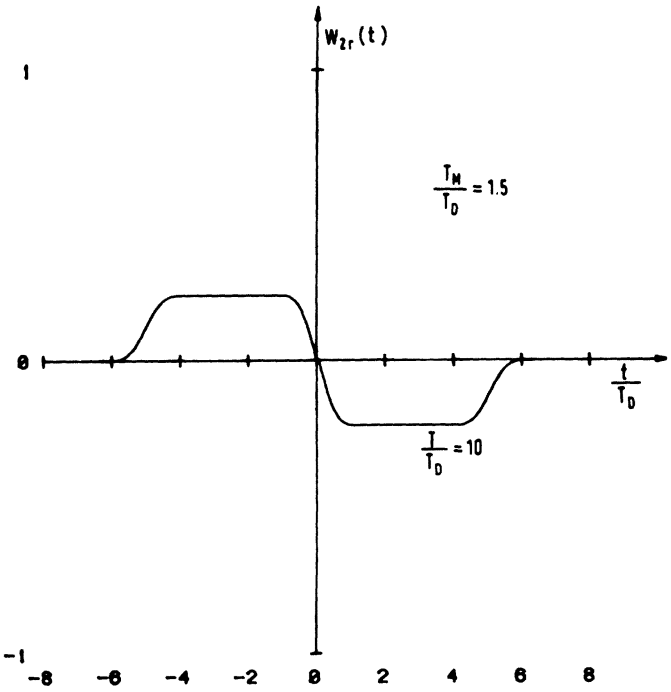

Fig. 6.7. Calculated filter outputs $W_{2r}(t)$ for T_M/T_D = 1.5 and with several T/T_D values.

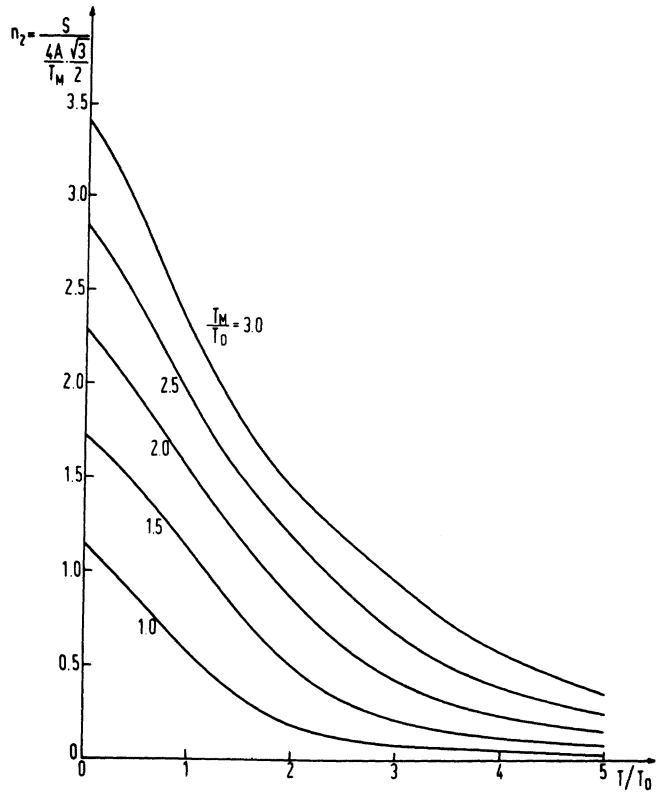

Fig. 6.8. Normalized zero crossing slope n_2 calculated for the voltage filter outputs $W_{2r}(t)$ (Fig. 6.7), with $F_r(t)$ as input pulses.

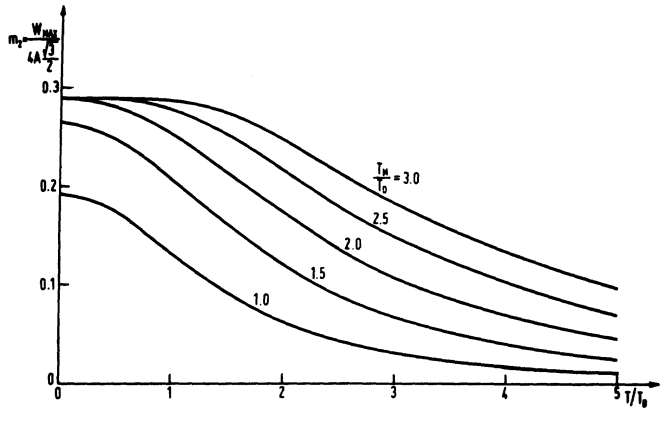

Fig. 6.9. Normalized peak amplitude m_2 of the voltage filter output $W_{2r}(t)$ (Fig. 6.7), with $F_r(t)$ as input pulses.

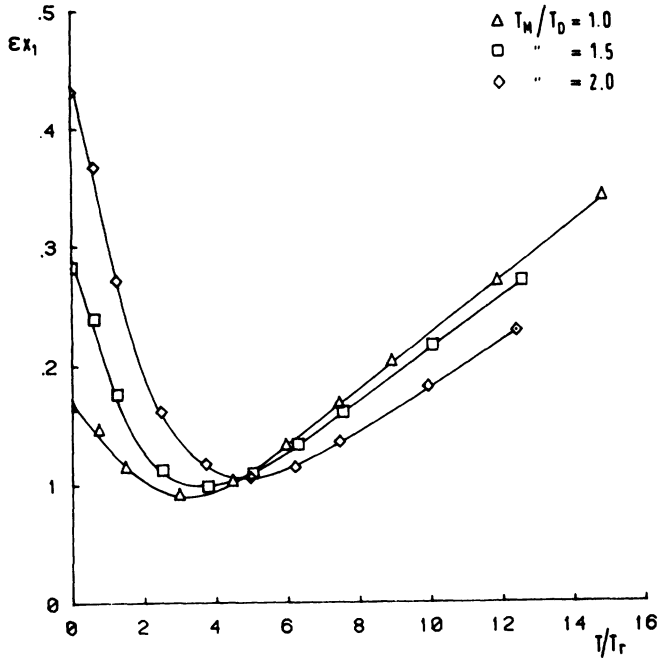

Fig. 7.1. Space resolution in mm in the drift (x) direction when using the first filter, as a function of $\lambda = T/T_r$, for three different values of T_M/T_D.

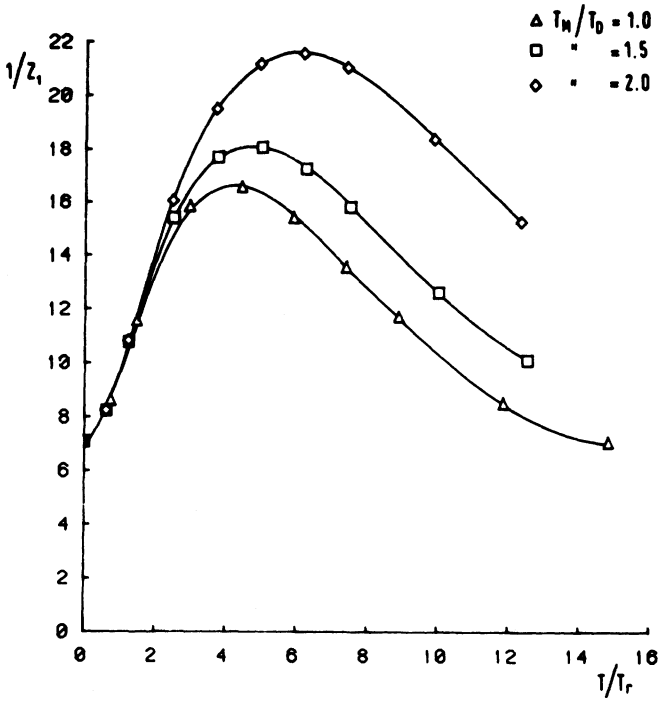

Fig. 7.3. Signal to noise ratio when using the first filter as a function of $\lambda = T/T_r$, for three different values of T_M/T_D.

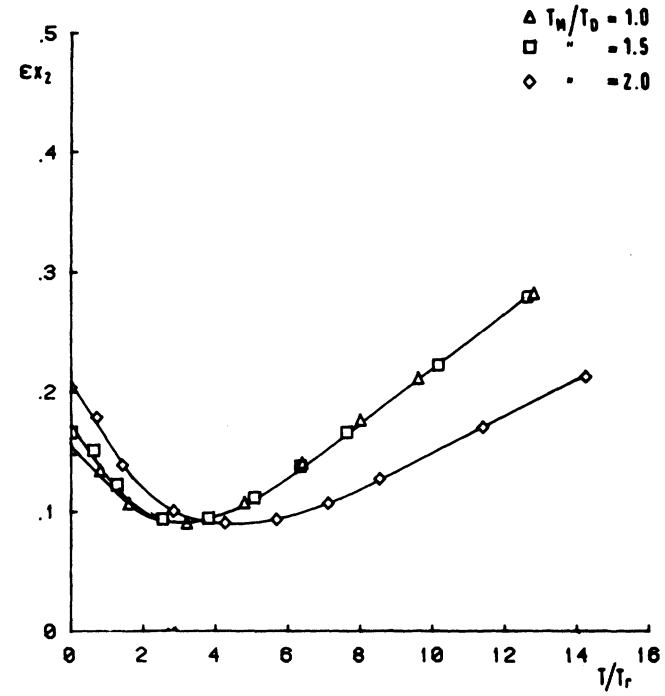

Fig. 7.2. Space resolution in mm in the drift (x) direction when using the second filter, as a function of $\lambda = T/T_r$, for three different values of T_M/T_D.

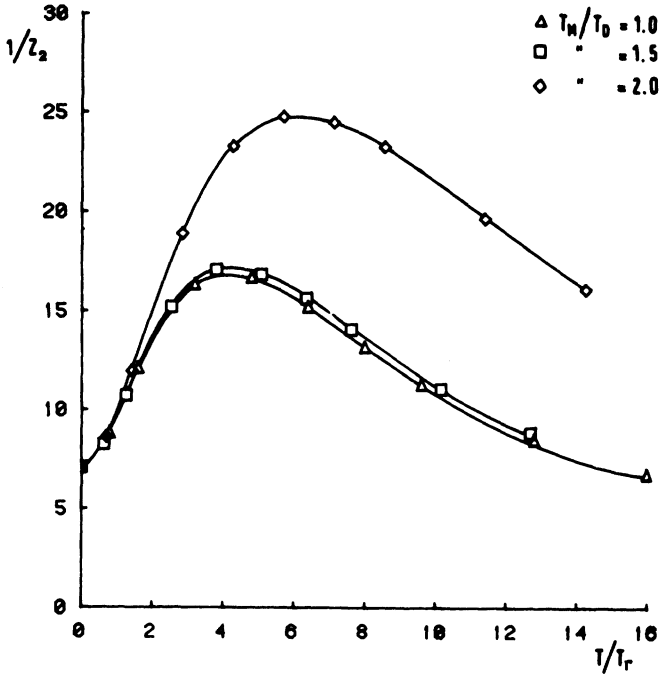

Fig. 7.4. Signal to noise ratio when using the second filter as a function of $\lambda = T/T_r$, for three different values of T_M/T_D.

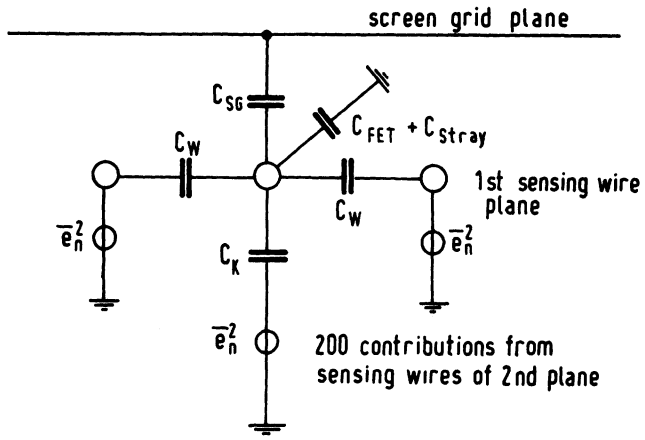

$C_{SG} = 0.96$ pF

$C_W = 1.323$ pF

$200\,C_K = 1.02$ pF

Fig. 8.1. Equivalent circuit for input capacitances and noise sources at the amplifier input.